Air Force Institute of Technology
AFIT Scholar

Theses and Dissertations

Student Graduate Works

3-21-2013

Laser Illuminated Imaging: Multiframe Beam Tilt Tracking and Deconvolution Algorithm

David J. Becker

Follow this and additional works at: https://scholar.afit.edu/etd

Part of the Other Electrical and Computer Engineering Commons

LASER ILLUMINATED IMAGING: MULTIFRAME BEAM TILT
TRACKING AND DECONVOLUTION ALGORITHM

THESIS

David J. Becker, Captain, USAF

AFIT-ENG-13-M-07

DEPARTMENT OF THE AIR FORCE
AIR UNIVERSITY

AIR FORCE INSTITUTE OF TECHNOLOGY

Wright-Patterson Air Force Base, Ohio

AFIT-ENG-13-M-07

LASER ILLUMINATED IMAGING: MULTIFRAME BEAM TILT TRACKING AND
DECONVOLUTION ALGORITHM

THESIS

Presented to the Faculty

Department of Electrical and Computer Engineering

Graduate School of Engineering and Management

Air Force Institute of Technology

Air University

Air Education and Training Command

In Partial Fulfillment of the Requirements for the

Degree of Master of Science in Electrical Engineering

David J. Becker, BS

Captain, USAF

March 2013

AFIT-ENG-13-M-07

LASER ILLUMINATED IMAGING: MULTIFRAME BEAM TILT TRACKING AND
DECONVOLUTION ALGORITHM

David J. Becker, BS
Captain, USAF

Approved:

_____   _____
Dr. Stephen C. Cain, PhD (Chairman)   Date

_____   _____
Lt Col James A. Louthain, PhD (Member)   Date

_____   _____
Maj Patrick S. Chapin, PhD (Member)   Date

AFIT-ENG-13-M-07

Abstract

A laser-illuminated imaging system operating in the presence of atmospheric turbulence will encounter several sources of noise and diffraction induced errors. As the beam propagates, turbulence induced tilt will cause the beam to wander off axis from the target. This is especially troublesome when imaging satellites, since most turbulence is closer to the Earth's surface and greatly affects the beam in the early stages of propagation. Additionally, the returning beam convolved with the target will encounter turbulence induced tilt that appears as apparent movement of the target between image frames. This results in varying beam intensities at the target surface between imaging frames that can affect registration algorithms and tracking. In this research effort, an algorithm using expectation maximization and least squares techniques was developed that has the ability to separately estimate both the tilt of the pulsed laser beam and the apparent movement of the object between incoherent frames and produce a superior image estimate of the target and provide tracking information. The results from this algorithm can be used to reduce the effects of beam wander and increase the SNR of post-processed images.

Table of Contents

List of Abbreviations

Laser Illuminated Imaging:
Multiframe Beam Tilt Tracking and
Deconvolution Algorithm

I. Introduction

This chapter describes the problem to be addressed by this research, the goals of this project and previous related efforts. Additionally, the assumptions used in this research on the system and its data are examined in order to limit the scope of the problem. Lastly, an outline for the organization of this thesis is given.

1.1 Problem Statement

When obtaining high resolution images from a *laser detection and ranging* (LADAR) system there are several factors that limit the systems performance investigated in this research, such as diffraction due to the optics, atmospheric turbulence and laser beam speckle. These factors can severely distort the image quality and reduce the resolution of the measured data. Due to operating conditions and factors such as cost, size and weight, an adaptive optics approach may not be feasible for all situations. This is where the benefits of a post-processing algorithm can be exploited to improve the quality of LADAR obtained imagery. The proposed algorithm is capable of providing estimates of the target image with distortions such as speckle, blurring and defocus mitigated via a multiframe processing strategy.

Atmospheric turbulence causes random time delays in light as it propagates through the atmosphere. In a LADAR application, diffraction due to the atmospheric turbulence results in tilt, blur, defocus and other distortions to the image. Of these

distortions, tilt accounts for 87% of the error [14]. Using a Fourier optics approach this time delay or tilt in the propagation field can be represented as a spatial shift in the image field [9]. Thus, each pulse of the laser beam is randomly shifted to a different position on the target and the returning field after propagation is again shifted and blurred. This shift in the image field is what a registration algorithm corrects for, which facilitates averaging multiple frames. Additionally, in a LADAR system, speckle is a significant source of noise. Speckle is caused by the coherency of the illuminating laser source combined with the rough surface of the target [10]. Each frame of data will contain independent intensity fluctuations that appear as bright and dark spots as a result of laser speckle. This noise further complicates the registration and averaging of multiple frames of an image set.

Current deconvolution and registration algorithms are successful in mitigating these effects however they do not take into account the effects of the illuminating beam shifting around due to turbulence known as beam wander. Current algorithms assume the beam is stationary for each frame of data. This is not a true assumption when propagating a beam in a turbulent atmosphere with a beam width at the target is smaller than the *field of view* (FOV) of the receiver optics.

1.2 Research Goals

The primary goal of this research is to derive and prove that when using a multiframe deconvolution *expectation maximization* (EM) algorithm that tracks and estimates the beam wander in each frame of an image set, the global shift or scene shift

estimate improves. The resulting registered image's spatial resolution will improve while also providing an estimate of the beam's position at each frame.

The potential increase in resolution of the post-processed image and the tracking information provided has both commercial and defense applications. Such applications include laser weapons that require tracking beam wander to focus a high energy laser on an intended target and remote tracking and imaging applications that involve a scene shifting independently from a shifting beam.

1.3 Assumptions

For this research, several assumptions of the situation were made to limit the scope of the project:

- The shape of the *point spread function* (PSF) due to the receiver optics and atmospheric turbulence is known or can be measured

- The size of the laser beam at the target is the factor limiting the FOV of the detected image

- The target is stationary across the set of images used by the algorithm

- The range to the target or the LADAR beam size at the target is known

- The mean background noise is known or can be measured

- The beam movement is small enough between frames so that the portion of the target being illuminated is not completely different than the other image frames

1.4 Thesis Organization

In this thesis, *Chapter II* provides the background and theory needed to understand the concepts in this research. Additionally *Chapter II* explains the effects of beam wander on current image registration algorithms. *Chapter III* describes the

mathematical derivation of the proposed algorithm, along with the simulation and the laboratory set-up developed to evaluate the algorithm. *Chapter IV* details the results and provides an analysis from testing the algorithm using the experimental set-up and the simulation described in *Chapter III*. Lastly, *Chapter V* gives a summary of the research, provides conclusions on the thesis and offers opportunities for future work to expand this effort.

II. Background & Theory

This chapter provides an overview of the technical background material necessary for understanding the concepts of this research. A brief description of a LADAR system and the issues that affect the image quality and the ability to process these images is provided. A brief review is conducted on different deconvolution algorithms that have been developed and their limitations to the addressed problem. The effects of beam wander on the most common image registration algorithm is illustrated and discussed. Additionally, several image registration techniques that are quick to implement and execute are discussed.

2.1 LADAR System Model

The generic LADAR imaging system represented in this research interrogates a target using a coherent pulsed laser. If the light is coherent, it is assumed that the phase of the laser beam is constant over the integration time of the camera. Once the target is illuminated by the laser beam, the beam reflects off the target and the returning pulse goes through the LADAR optics systems to form an image. This basic system description is illustrated in Figure 1. As discussed later in this chapter, the propagation path between the LADAR system and the target contains atmospheric turbulence that adversely affects the detected image's quality.
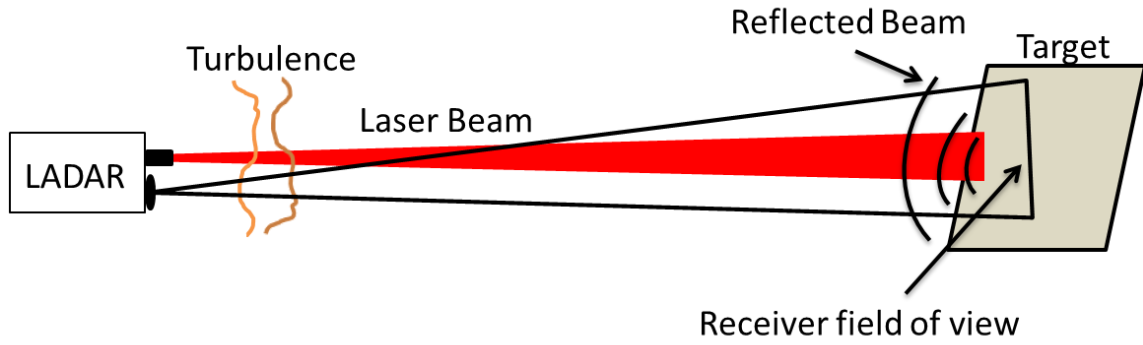
Figure 1: Basic LADAR system concept

Using Fourier optics, a basic model for the image obtained by the system, i, is described in Equation 1, where o is the target multiplied by the illuminating beam, b, convolved with, h, the PSF. In this equation, the detector plane coordinates are represented as x and y while the coordinate system at the target is in the z, w plane. The two reference planes are considered to be square with N pixels in each direction.

$$i(x,y) = \sum_{z}^{N}\sum_{w}^{N} o(z,w)b(z,w)h(x-z,y-w) \tag{1}$$

The PSF or the impulse response describes the response of the system to a point source and includes the effects of the imaging system and the atmosphere. This research assumes that the PSF is known or can be measured. By definition the *optical transfer function* (OTF) abbreviated as $H(f_x, f_y)$ is simply the Fourier transform of the PSF. The variables f_x and f_y represent the spatial frequencies of the OTF in two dimensions.

There are several scenarios for how the beam interacts with the target as shown in Figure 2. These are dependent on the optics of the LADAR system and the size of the beam at the target. It is possible that the target is flood illuminated, meaning the beam is larger than the target and the FOV is larger than the target, thus the entire scene is

illuminated and imaged. Another possibility is that the receiver optics FOV is limiting the detected image thus the entire detected image is illuminated but only a portion of the scene is measured by the optics. The third possibility, and the one used in this research, is that the beam size at the target is both smaller than the actual target and the FOV of the receiver optics. Several important factors limit the performance of the LADAR system during this process including atmospheric turbulence, noise and coherent laser speckle. Each of these factors is discussed in detail below.
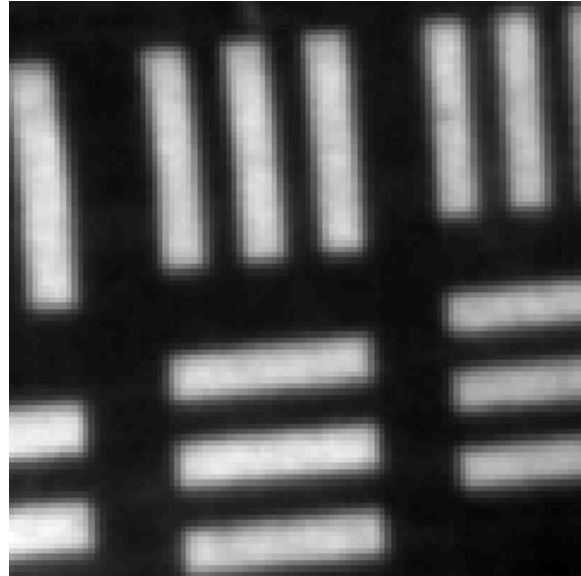
(a)   (b)
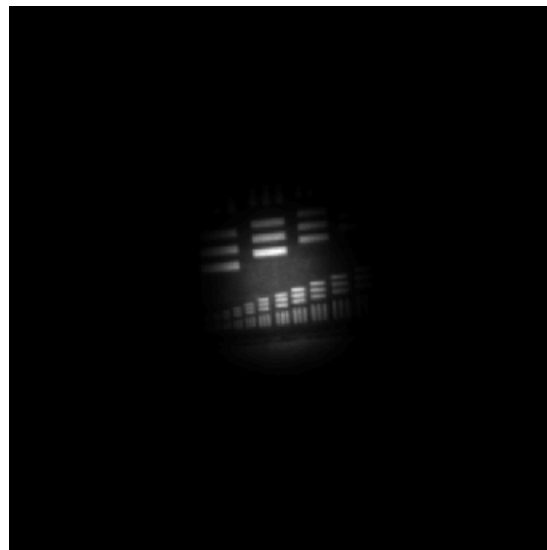
(c)

**Figure 2: Detected image limiting factors: (a) Flood illuminated limited. (b) Detector FOV limited.
(c) Beam width limited.**

2.2 Noise

The majority of noise in a LADAR system can be attributed to one of the following sources: photon counting noise, laser speckle and background noise [13]. Each

of these noise sources additively contribute to lowering the *signal-to-noise ratio* (SNR) of the detected image and thus affecting the performance of any post-processing algorithms.

2.2.1 Photon Counting Noise

Photon noise or shot noise is a result of the *charge coupled device* (CCD) array in the LADAR system's camera being a discrete device that counts the number of photons that arrive at each element of the array [1]. The distribution of the photons is modeled as a Poisson process where photons arrive at random intervals with a mean number of photons, λ, arriving over a set time interval. The mean is also a random process that will differ from frame to frame. The probability of r photons being counted at a pixel spot is given by the Poisson *probability mass function* (PMF) shown in Equation 2. Due to photon noise, the same target imaged at two different times will not have the same intensity at each pixel spot creating an uncertainty in the pixel value between two different frames of data.

$$\text{P}(r) = \frac{\lambda^r e^{-\lambda}}{r!} \tag{2}$$

2.2.2 Speckle Noise

Speckle noise caused by the coherent nature of the laser in the LADAR system is usually the largest source of noise [13]. Laser speckle is the result of imaging a surface, rough on the scale of an optical wavelength, using the coherent light from a laser. Considering that the optical wavelength in a LADAR system is around 1μm, the variation in the surface roughness can be as small as 1μm and cause significant phase change in the measured light at the detector from each point on the target. As illustrated in Figure 3,

when this incoming light field is randomly delayed due to the rough surface, their sums can interfere with one another causing bright and dark spots [5]. Dark spots would occur due to deconstructive interference when the phases of the fields cancel each other out. Constructive interference resulting in bright spots would occur when the fields arrive in phase and increase the intensity level. According to work by Dr. Goodman [10], speckle is a double stochastic process in that the intensity fluctuations follow a Gamma distribution with a certain number of degrees of freedom related to the coherency of the illuminating light. This is combined with Poisson photon counting, resulting in a negative binomial distribution.
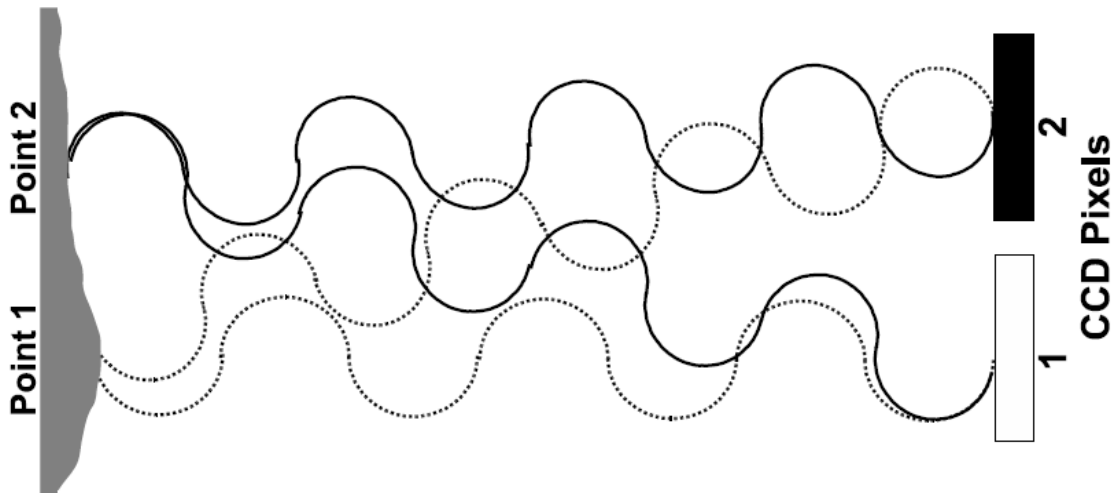
Figure 3: Illustration of phase coherency and speckle noise due to a rough target.

The variance of the laser speckle, shown in Equation 3, represents that of a negative binomial distribution [13] and is dependent on the coherency of the light and the expected number of photons received. An example of speckle phenomenon is shown in

Figure 4, the image has a random intensity modulation that severely distorts the image quality when compared to the image obtained from an incoherent light source.

$$\sigma^2_{speckle} = E[N_{signal}]\left(1 + \frac{E[N_{signal}]}{\bar{\mu}}\right)$$ (3)

Where,
- $E[N_{signal}]$ is the expected number of photons
- $\bar{\mu}$ is the coherency factor of the light, 1 = fully coherent, ∞ = fully incoherent
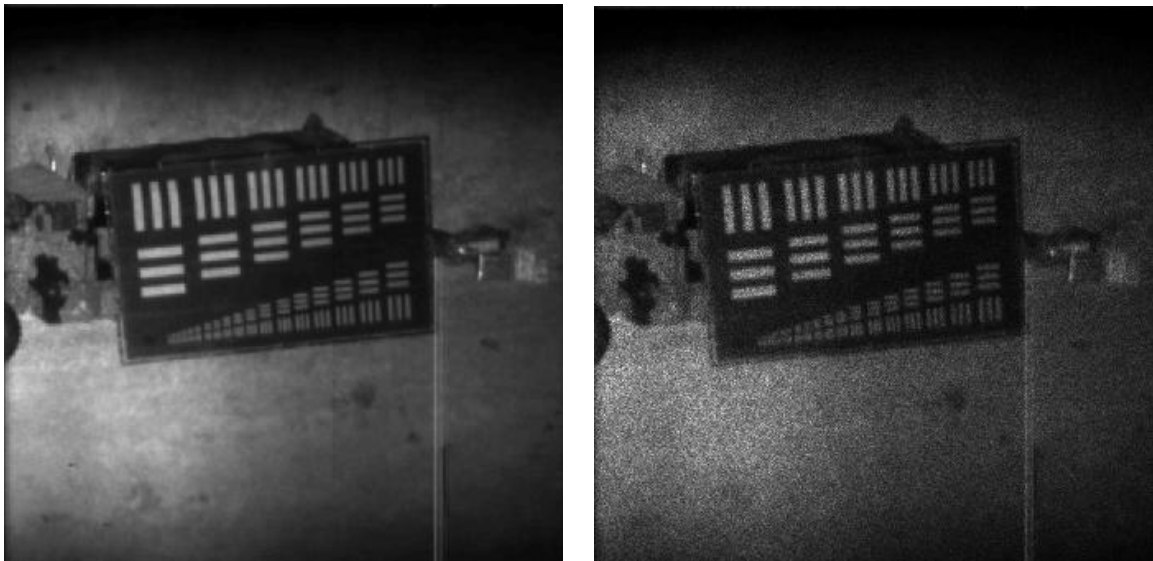
(a)   (b)

Figure 4: Speckle noise illustration: (a) Incoherent illuminated image. (b) Coherent illuminated image.

Speckle noise can be mitigated by using a time average of properly registered images [2]. Depending on the coherence of the light, the speckle pattern introduced to each image can be especially troublesome when registering multiple frames. If image quality is poor, an algorithm might not properly register each image frame and will blur the averaged result. However, a deconvolution algorithm used to remove the effects of

the atmosphere should be able to improve the quality because the blurring effect from improperly registered frames is similar to the blurring effect caused by the atmosphere.

2.2.3 Background Noise

Background noise is the result of any light or signal aside from the illuminating beam that is measured by the detector [13]. There are various sources of background noise and many are dependent on the situation, they include but are not limited to the sun, starlight, city lights and the laser light reflecting off other surfaces and bouncing back to the detector. In some situations, it is possible to estimate the amount of background by taking images with the illuminating laser turned off to get a mean background light level.

2.3 Atmospheric Turbulence

Turbulence in Earth's atmosphere is caused by random variations in temperature and air motion that changes the refractive index of the air [12]. As optical waves propagate in Earth's atmosphere, the wave is distorted by the changes in the refractive index of the air it is traveling through causing phase shifts in the propagated wavefront, this is illustrated in Figure 5.
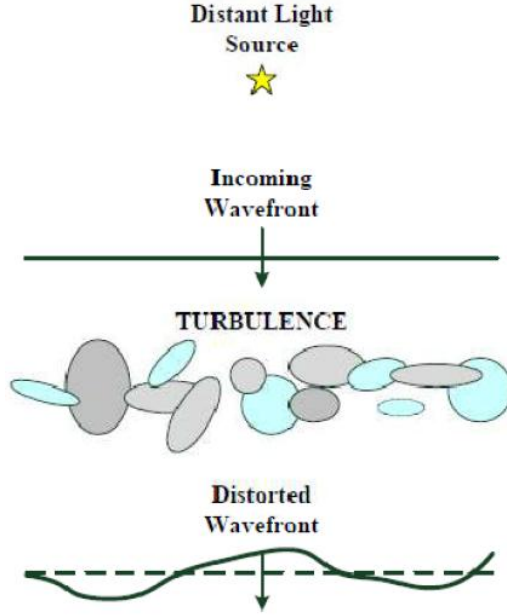
Figure 5: Effects of turbulence on a propagated wavefront [11].

Using Fourier optics and the shift theorem shown in Equation 4, a phase shift represented by the exponential term in the temporal domain introduces a spatial offset or translational shift (a, b) in each dimension of the spatial domain [9]. The terms in the equation, g and G represent a Fourier transform pair with G being the Fourier transform of g.

$$\Im\{ g(x - a, y - b)\} = G(f_x, f_y)e^{-j2\pi(f_x a + f_y b)}$$

(4)

The total variance in the phase of the wavefront field as a result of turbulence is described by Equation 5, where D is the diameter of the receiver aperture and r_0 is the coherence diameter or Fried's seeing parameter [10]. The coherence diameter or seeing parameter is used to describe the optical quality of the atmosphere and is typically around 5-10 cm for average viewing sites and up to 20 cm for the best viewing sites.

13

$$\sigma^2 = 1.03 \left(\frac{D}{r_0}\right)^{5/3} \tag{5}$$

The phase variance due to tilt [14], in one axis is given by Equation 6, this variance is doubled when looking at both axis. Nearly 87% of the total phase variance is a result of tilt with image distorting effects such as blurring and defocus making up the rest. Tilt can be mitigated by an accurate image registration algorithm. With tilt removed, the residual phase variance, given in Equation 7, represents the higher order image distortions such as defocus that are corrected for using a deconvolution algorithm. Shown here is the phase variance in the one dimensional θ direction. These equations would be identical for each of the translation shifts axes.

$$\sigma_\theta^2 = 0.448 \left(\frac{D}{r_0}\right)^{5/3} \tag{6}$$

$$\sigma^2_{tilt\ removed} = 0.134 \left(\frac{D}{r_0}\right)^{5/3} \tag{7}$$

The atmospheric turbulence interacts with the beam causing random phase delays and results in a beam that has been shifted off axis from the intended target. The turbulence will also introduce distortions in the beam intensity at the target known as beam breathing and beam scintillation [8], however these effects were not studied in this research. The returning field is affected in the same way with atmospheric turbulence resulting in tilt, blur and other higher order distortions on the returned image. Using the Fourier shift theorem previously shown in Equation 4, the phase delay or wavefront tilt in the reflected image translates to a global spatial shift in the detected image. Taking into

14

account the beam shift and global shift introduced by the turbulent atmosphere, an update to Equation 1, which was an expression for the image obtained from a LADAR system, is shown in Equation 8. In this equation, i_k, is the kth measured data frame in a given set. The global shifts for each kth frame of data are represented in the PSF as translational shifts α_k and β_k in the detector plane coordinate system x and y. The beam shifts are represented as γ_k and ε_k in the target plane coordinate system z and w.

$$i_k(x,y) = \sum_{z}^{N} \sum_{w}^{N} o(z,w)b(z - \gamma_k, w - \varepsilon_k)h(x - z - \alpha_k, y - w - \beta_k) \tag{8}$$

Equation 8 implies that each frame of data obtained from an image set with a stationary target will contain both a beam that has shifted thus illuminating a different location on the target. Additionally, the target has an apparent movement from the previous frame due to the global shift introduced in that frame. This is illustrated in Figure 6 with simulated sequential data frames that show the effects of turbulence induced independent shifting on the illuminating beam and the global scene.

<center>(a)   (b)</center>
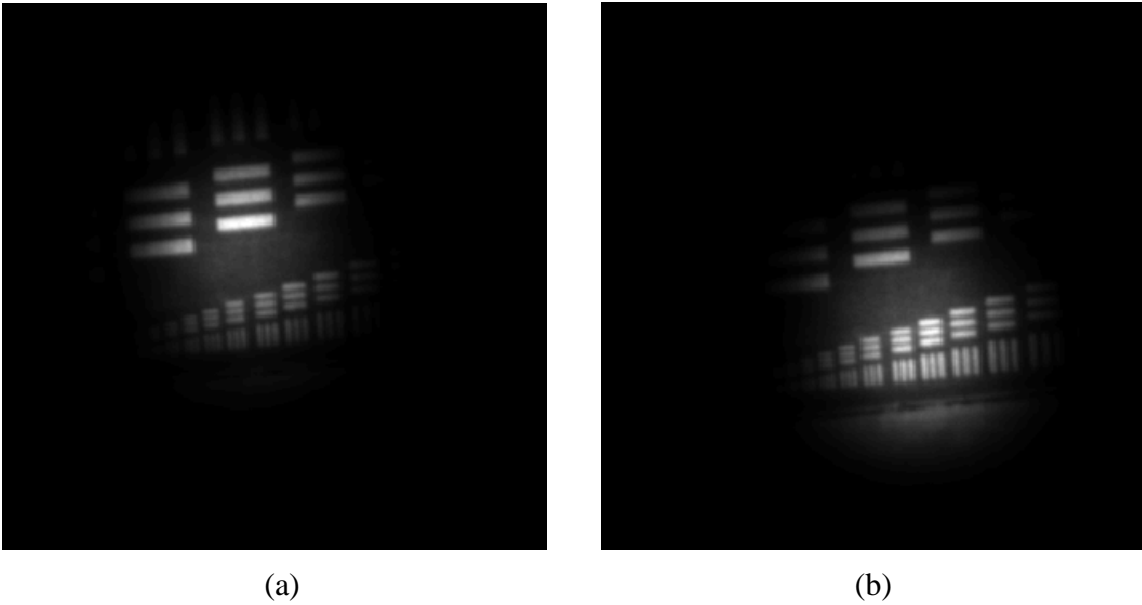
Figure 6: Effects of turbulence induced tilt on beam and scene: (a) Frame 1. (b) Frame 2.

The amount of tilt in each frame is not necessarily statistically uncorrelated and independent from the previous frame or time instance. There is a degree of correlation in the amount of tilt that needs to be considered in order to accurately model the temporal characteristics of atmospheric induced tilt. The tilt correlation function with details found in [13] is dependent on the characteristics of the LADAR system such as the time between pulses and the size of the aperture, as well as the degree of turbulence and the wind speeds at the imaging site. As the wind speed increases, the correlation in the atmospheric turbulence phase screen decreases to a point where there is zero tilt correlation at each frame of data.

2.4 Image Registration

Image registration is the process that compares and aligns multiple images by estimating the spatial relationship between them. Typically these relationships could be described by simple translation (horizontal and vertical shifts), rotational, or scaling differences. Only translation shifts were evaluated in this research. Proper registration is vital to obtaining averaged images that have a sufficient SNR for further post-processing the data and making it usable for many applications.

There are many image registration techniques, several of which are identified and compared in [2]. Some common methods include cross-correlation, directional searching and block matching. This research utilizes a version of the directional search method in which the *sum of squared errors* (SSE) cost function is iteratively evaluated in four translational shift step directions (up, down, left and right or respectively positive y, negative y, negative x and positive x). The search continues until the SSE cost function is minimized. This approach is susceptible to a local minimum value, but in this application the search area is minimized by the limitation on the variance of the beam shift and global shift as previously discussed.

The benefits of proper image registration are illustrated in Figure 7. When multiple frames of speckled data similar to that shown in Figure 4 are averaged but not registered correctly, the speckle noise is reduced; however the image is significantly blurred due to the motion between frames not being corrected. If the images are perfectly registered as shown in Figure 8, averaging speckled frames of data removes the speckle noise and results in a much higher resolution image. It is evident that proper registration is of significant importance when dealing with coherent based imaging systems.
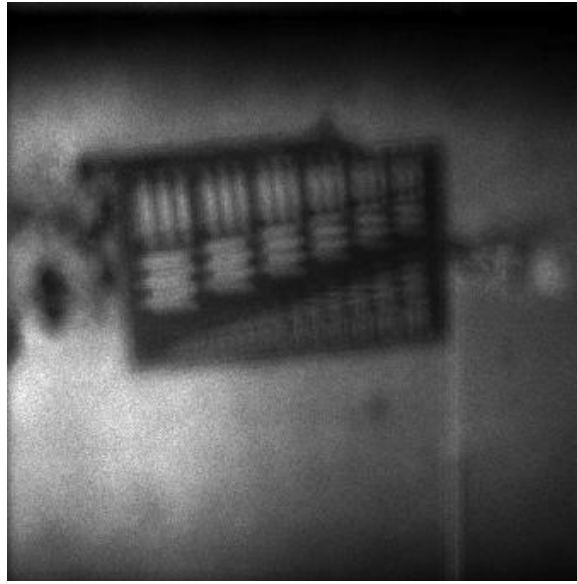
Figure 7: Example of improper image registration when averaging 10 speckled frames

Figure 8:   Example of perfect image registration when averaging 10 speckled frames

Missing from these algorithms is the ability to register multiple frames of data while tracking and incorporating a beam that has shifted positions at each individual

frame. To illustrate this, a cross-correlation algorithm was used to register multiple frames of data [2]. In one scenario, the illuminating beam was stationary as is the assumed case in all the algorithms previously mentioned. In another scenario, beam wander was introduced to each frame. The results in Figure 9 and Figure 10 show that the pixel error in each dimension (*x* and *y*) was considerably greater when beam wander was present compared to a stationary beam. The difference in the error between these two figures is likely a result of the properties of the simulated target and not a result of the algorithm. These results illustrate the purpose of this research. Preliminary simulations show that beam wander causes significant registration errors in common image registration techniques. If beam wander can be estimated in each frame and corrected for, its effect on registration can possibly be decreased.
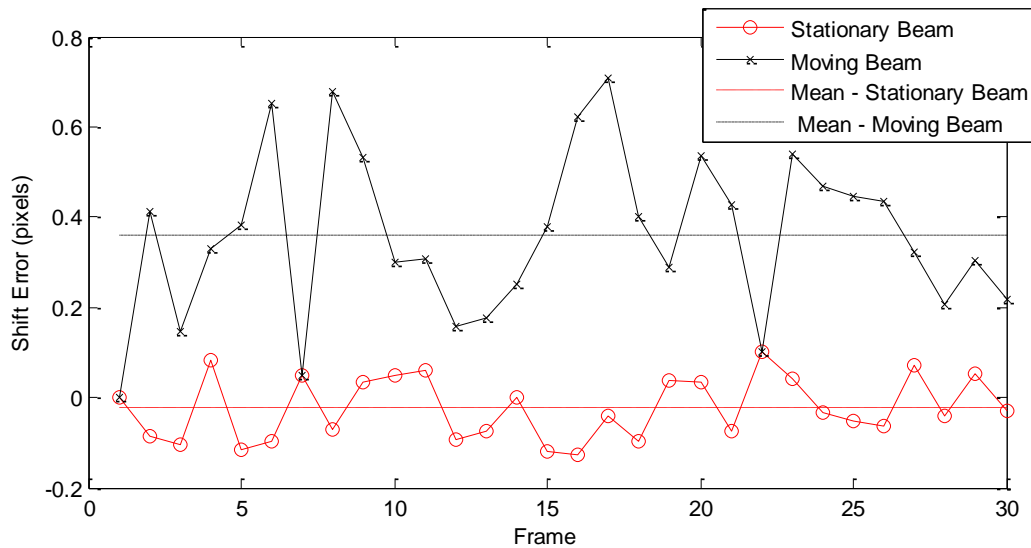
Figure 9:   Cross correlation registration error with and without beam wander in the x direction

19
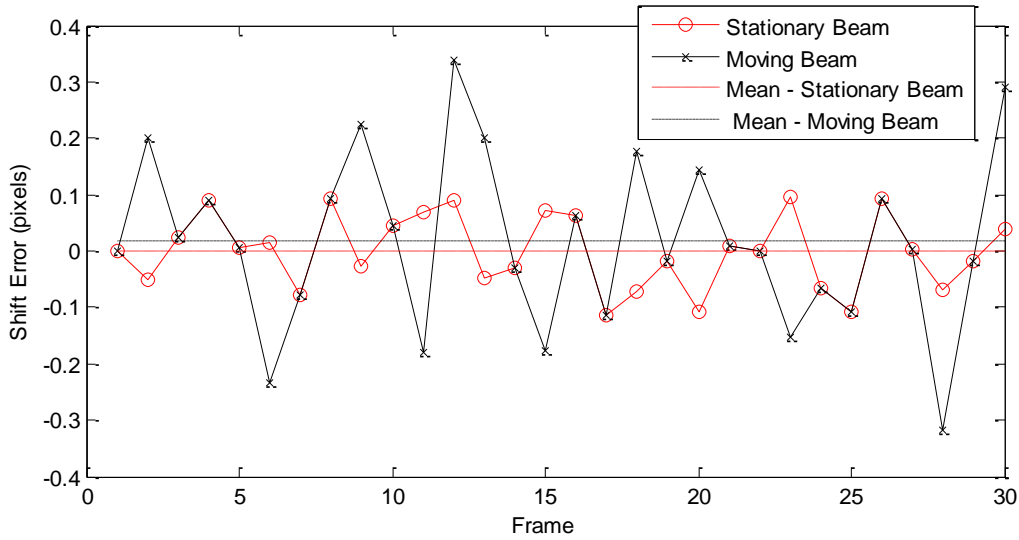
Figure 10: **Cross correlation registration error with and without beam wander in the y direction**

2.5 Deconvolution Algorithms

A deconvolution algorithm, in which diffraction and distorting effects of the atmosphere and optical system are removed, is equally important to obtaining high resolution and quality post-processed images. Deconvolution, unlike the more difficult blind deconvolution, assumes these affects are known or can be measured through knowledge of the PSF. Several of the most common algorithms found in image processing include the Ayers-Dainty blind deconvolution technique [7] and the *multi-frame blind deconvolution* (MFBD) algorithm [4]. The MFBD algorithm is an iterative EM approach to computing the maximum likelihood estimate of the unknown parameters. A benefit when working with EM algorithms is that their convergence is assured since the algorithm is guaranteed to increase the likelihood function at each

iteration. Again, missing from both these algorithms is the ability to track a wandering

beam in each frame of data and then use that information to improve the deconvolution

capability of the algorithm.

III. Methodology & Testing

The proposed approach to reduce the effects of the atmospheric turbulence and speckle noise of imagery obtained from a LADAR system is to develop an EM algorithm that estimates the global shift and the beam shift in each frame independently. This chapter describes the mathematics in developing this algorithm and the implementation issues with the EM solution. An alternate solution is proposed based on proven algorithms that can provide superior performance. An overview of the simulated and measured data is given along with criteria that will be used to test if the proposed algorithm results in greater performance.

Throughout the derivations in this section, all equations are written using a one dimensional coordinate system. This compresses the lengthy equations that can be easily generalized into two dimensions. The complete two dimensional equations are given in the final step of the derivation.

3.1 Expectation Maximization

The EM algorithm is an iterative approach to computing the maximum-likelihood estimate of the unknown parameters in a given data set. Similar to many deconvolution algorithms, the EM deconvolution algorithm proposed in this research is derived using Poisson statistics. Poisson statistics have the following properties that make working with them mathematically simple [6]:

- The mean of a Poisson process is equal to its variance

- The sum of multiple independent Poisson distributions is another Poisson distribution with its mean equal to the sum of the means

Following the steps outlined by Dempster, Liard and Rubin [3], an EM algorithm is proposed to iteratively estimate the unknown parameters that maximize the expected log-likelihood function.

3.1.1 Statistical Model for the Incomplete Data

Defining a statistical model for the incomplete data, which is the observed or measured data, is the first step in formulating an EM deconvolution algorithm. This model is defined in Equation 9. It is known that the incomplete data, d, is an image array of independent Poisson random variables containing the true target image, o, multiplied by the beam, b, with an unknown translational shift, γ, and convolved with a PSF, h, that contains a global translational shift, α. The measured background radiation is represented as B in Equation 9. Notice that each frame, k, contains an independent shift in both the beam and global scene. The coordinate system used in the derivation of this algorithm is shown in Figure 11.

$$\mathrm{E}[d_k(x)] = \sum_z^N o(z)b(z - \gamma_k)h(x - z - \alpha_k) + B(x) \tag{9}$$
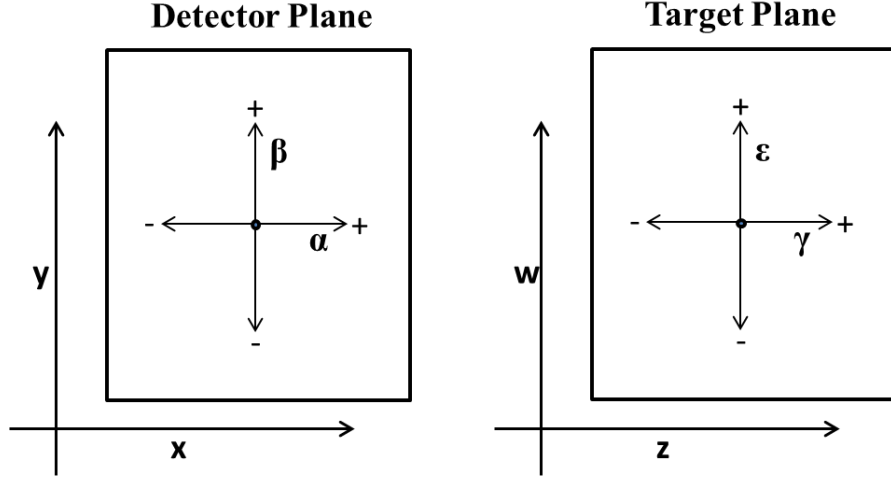
Figure 11: Defined coordinate system in the detector and target plane

3.1.2 Define the Complete Data

The complete data, $\widetilde{d}$, which is the diffraction and noise removed desired data has to be statistically related to the incomplete data previously defined in Equation 9. The relationship chosen between the two is shown below in Equation 10. Unlike the incomplete data, d_k, this quantity is not measureable and is estimated using the EM algorithm.

$$d_k(x) = \sum_{z}^{N} \widetilde{d_k}(x, z) + B(x) \tag{10}$$

3.1.3 Statistical Model for the Complete Data

A statistical model for the complete data is defined so that the relationship expressed in Equation 10 produces the correct statistical model for the incomplete data. If the complete data is considered to be set of Poisson random variables, the incomplete data can be related to the complete data through Equation 11. Choosing the complete

data to be Poisson is acceptable because the sum of Poisson random variables is also a

Poisson random variable [10].

$$E[\widetilde{d_k}(x,z)] = o(z)b(z - \gamma_k)h(x - z - \alpha_k) \tag{11}$$

The statistical model for the complete data is verified through the mathematical

equivalence expressions in Equation 12. Starting with Equation 10, the expected value is

taken and the relationship in Equation 11 is substituted in. This result is equivalent to the

relationship defined in Equation 9.

$$d_k(x) = \sum_z^N \widetilde{d_k}(x,z) + B(x)$$

$$E[d_k(x)] = E\left[\sum_z^N \widetilde{d_k}(x,z)\right] + B(x) = \sum_z^N E[\widetilde{d_k}(x,z)] + B(x) \tag{12}$$

$$E[d_k(x)] = \sum_z^N o(z)b(z - \gamma_k)h(x - z - \alpha_k) + B(x)$$

3.1.4 Formulate the Complete Data Log-Likelihood

Using the Poisson PMF previously shown in Equation 2 and applying the model

for the complete data defined in Equation 11, results in the complete data likelihood

expression:

$$P[\widetilde{d_k}(x,z)] = \frac{o(z)b(z - \gamma_k)h(x - z - \alpha_k)^{\widetilde{d_k}(x,z)}e^{-o(z)b(z-\gamma_k)h(x-z-\alpha_k)}}{\widetilde{d_k}(x,z)!} \tag{13}$$

The next step is to expand Equation 13 by solving for all pixel points (x, z) across

the image set containing K frames. This produces the joint probability for the complete

data likelihood shown in Equation 14. Due to the independence of each pixel and frame,

the PMFs for each pixel point and frame of data are simply the product of the individual

PMFs [6].

$$P[\widetilde{d_k}(x,z) \ \forall \ x,z] = \prod_k^K \prod_x^N \prod_z^N \frac{o(z)b(z-\gamma_k)h(x-z-\alpha_k)^{\widetilde{d_k}(x,z)}e^{-o(z)b(z-\gamma_k)h(x-z-\alpha_k)}}{\widetilde{d_k}(x,z)!} \tag{14}$$

Following the EM derivation steps, the natural log of Equation 14 is taken to get

the log-likelihood function, *L*, shown in Equation 15. The log-likelihood function is

defined by the unknown parameters in the complete data (o, α_k, γ_k). Greatly simplifying

this equation is that the natural log of the product operator on multiple expressions is a

much simpler summation operator on each expression individually.

$$L(o, \alpha_k, \gamma_k) = \sum_k^K \sum_x^N \sum_z^N \widetilde{d_k}(x,z) \ln\big(o(z)b(z-\gamma_k)h(x-z-\alpha_k)\big)$$
$$- o(z)b(z-\gamma_k)h(x-z-\alpha_k) - \ln\big(\widetilde{d_k}(x,z)!\big) \tag{15}$$

3.1.5 Expectation of the Complete Data Log-Likelihood

The expectation step of the EM algorithm takes the conditional expectation of the

complete data log-likelihood derived in Equation 15 when given the incomplete data and

previous or old estimates of the unknown parameters (o, α_k, γ_k). The conditional

expectation is calculated and shown below in Equation 16.

26

$$E\left[\left(L(o,\alpha,\gamma)\big|\hat{o}^{old},d_k(x),\alpha_k^{old},\gamma_k^{old}\right)\right]$$

$$= E\left[\sum_k^K \sum_x^N \sum_z^N \widetilde{d_k}(x,z)\ln\big(o(z)b(z-\gamma_k)h(x-z-\alpha_k)\big) - o(z)b(z-\gamma_k)h(x-z-\alpha_k)\right.$$

$$\left. - \ln\big(\widetilde{d_k}(x,z)!\big)\,|\hat{o}^{old},d_k(x),\alpha_k^{old},\gamma_k^{old}\right] \tag{16}$$

$$= \sum_k^K \sum_x^N \sum_z^N E\big[\widetilde{d_k}(x,z)\ln\big(o(z)b(z-\gamma_k)h(x-z-\alpha_k)\big)|\hat{o}^{old},d_k(x),\alpha_k^{old},\gamma_k^{old}\big]$$

$$- E\big[o(z)b(z-\gamma_k)h(x-z-\alpha_k)|\hat{o}^{old},d_k(x),\alpha_k^{old},\gamma_k^{old}\big] - E\big[\ln\big(\widetilde{d_k}(x,z)!\big)|\hat{o}^{old},d_k(x),\alpha_k^{old},\gamma_k^{old}\big]$$

Due to the linearity of the conditional expectation function, each term in the conditional expectation in Equation 16 can be evaluated independently.

First Term

The first term in the conditional expectation can be simplified by moving all the terms that are not dependent on the conditional parameters outside of the expectation function. The second step in simplifying this term is to recognize that this conditional expectation is related to the binomial PMF, this derivation is given in Appendix A. The final form for the first term is shown in Equation 17. The term, i_k^{old}, given in Equation 18, is the estimate of the image based on the past estimates of the unknown parameters.

$$E\big[\widetilde{d_k}(x,z)\ln\big(o(z)b(z-\gamma_k)h(x-z-\alpha_k)\big)\mid \hat{o}^{old},d_k(x),\alpha_k^{old},\gamma_k^{old}\big]$$

$$= E\big[\widetilde{d_k}(x,z)|\hat{o}^{old},d_k(x),\alpha_k^{old},\gamma_k^{old}\big]\ln\big(o(z)b(z-\gamma_k)h(x-z-\alpha_k)\big) \tag{17}$$

$$= \frac{\hat{o}^{old}(z)b\big(z-\gamma_k^{old}\big)h\big(x-z-\alpha_k^{old}\big)d(x)}{i_k^{old}(x)}\ln\big(o(z)b(z-\gamma_k)h(x-z-\alpha_k)\big)$$

Where,

$$i_k^{old}(x) = \sum_z^N \hat{o}^{old}(z)b\big(z-\gamma_k^{old}\big)h\big(x-z-\alpha_k^{old}\big) \tag{18}$$

Second Term

Similarly, the second term in the conditional expectation can be simplified. This term is not a function of any of the unknown parameters and thus all the terms can be brought outside of the expectation function. This term cannot be dropped, even though it is not dependent on the conditional parameters. Its value is not constant and will change at each iteration as the estimate of o is updated. Simplifying leads to the final form shown in Equation 19.

$$E\left[o(z)b(z-\gamma_k)h(x-z-\alpha_k)|\hat{o}^{old}, d_k(x), \alpha_k^{old}, \gamma_k^{old}\right] = o(z)b(z-\gamma_k)h(x-z-\alpha_k) \tag{19}$$

Third Term

The final term in the conditional expectation, containing the factorial operation, can thankfully be ignored. The term is not conditional on old estimates of the unknown parameters that are being estimated or the incomplete data. Thus this term is a constant value when maximizing the function with respect to the unknown parameters and does not need to be evaluated to maximize the complete data log-likelihood function.

Total Conditional Expectation

Combining the results of the three individual pieces of the conditional expectation, leads to the final form of the complete data log-likelihood conditional expectation, Q, shown in Equation 20.

$$Q = \mathrm{E}\left[\left(L(o,\alpha,\gamma)\big|\hat{o}^{old},d_k(x),\alpha_k^{old},\gamma_k^{old}\right)\right]$$

$$= \sum_k^K \sum_x^N \sum_z^N \frac{\hat{o}^{old}(z)b\left(z-\gamma_k^{old}\right)h\left(x-z-\alpha_k^{old}\right)d_k(x)}{i_k{}^{old}(x)} \ln\left(o(z)b(z-\gamma_{\tilde{k}})h(x-z-\alpha_k)\right) - o(z)b(z-\gamma_{\tilde{k}})h(x-z-\alpha_k)$$

$$= \sum_k^K \sum_x^N \sum_z^N \frac{\hat{o}^{old}(z)b\left(z-\gamma_k^{old}\right)h\left(x-z-\alpha_k^{old}\right)d_k(x)}{i_k{}^{old}(x)} \left(\ln\big(o(z)\big) + \ln\big(b(z-\gamma_{\tilde{k}})\big) + \ln\big(h(x-z-\alpha_k)\big)\right)$$

$$- o(z)b(z-\gamma_{\tilde{k}})h(x-z-\alpha_k) \tag{20}$$

3.1.6 Maximization of the Complete Data Log-Likelihood Conditional Expectation

With the conditional expectation known (Equation 20), the next step is to maximize it with respect to the parameters being estimated. This process is completed separately for the three different sets of unknown parameters: the global shift, the beam shift, and the true object. In each instance, the terms not dependent on the specific parameter being estimated can be dropped since they do not influence maximizing the function. The derivation for each of the three unknown parameter sets is given below individually.

<u>Maximize Global Shift</u>

When maximizing the conditional expectation from Equation 20 with respect to the global shift parameter (α_k), the terms that are not dependent on this parameter can be dropped as shown in Equation 21. Recognizing that the summed PSF term is constant for all values of shifts means that term can also be dropped. Since each frame contains a different shift, each frame is evaluated independently by setting $k = k_0$.

$$Q_\alpha = \sum_{k=k_0}^{N} \sum_{x}^{N} \sum_{z}^{N} \frac{\hat{o}^{old}(z)b(z-\gamma_k^{old})h(x-z-\alpha_k^{old})d_k(x)}{i_k^{old}(x)} \left(\cancel{\ln(o(z))} + \cancel{\ln(b(z-\gamma_k))}\right)$$

$$+ \ln\left(h(x-z-\alpha_k)\right)\right) - \cancel{o(z)b(z-\gamma_k)h(x-z-\alpha_k)} \tag{21}$$

$$= \sum_{x}^{N} \sum_{z}^{N} \frac{\hat{o}^{old}(z)b(z-\gamma_{k_0}^{old})h(x-z-\alpha_{k_0}^{old})d_{k_0}(x)}{i_{k_0}^{old}(x)} \ln\left(h(x-z-\alpha_{k_0})\right)$$

Thus, the final form of the maximum likelihood expression for the global shifts, Q_α, in a single given frame, k_0, after slight rearranging of terms is shown in Equation 22.

$$Q_{\alpha_{k_0}} = \sum_{z}^{N} \hat{o}^{old}(z)b(z-\gamma_{k_0}^{old}) \sum_{x}^{N} \frac{d_{k_0}(x)}{i_{k_0}^{old}(x)} h(x-z-\alpha_{k_0}^{old})\ln\left(h(x-z-\alpha_{k_0})\right) \tag{22}$$

Maximize Beam Shift

When maximizing the conditional expectation from Equation 20 with respect to the beam shift parameter (γ_k), the terms that are not dependent on this parameter can be dropped with the final form shown in Equation 23 having been slightly rearranged. Again, since each frame contains an independent shift, each frame is evaluated individually by setting $k = k_0$.

$$L_{\gamma_{k_0}} = \sum_{k=k_0}^{N} \sum_{x}^{N} \sum_{z}^{N} \frac{\hat{o}^{old}(z)b(z-\gamma_k^{old})h(x-z-\alpha_k^{old})d_k(x)}{i_k^{old}(x)} \left(\cancel{\ln (o(z))} + \ln (b(z-\gamma_k))\right)$$

$$+ \cancel{\ln (h(x-z-\alpha_k))} - o(z)b(z-\gamma_k)h(x-z-\alpha_k)$$

$$= \sum_{z}^{N} \hat{o}^{old}(z)b(z-\gamma_{k_0}^{old}) \ln \left(b(z-\gamma_{k_0})\right) \sum_{x}^{N} \frac{d_{k_0}(x)}{i_{k_0}^{old}(x)} h(x-z-\alpha_{k_0}^{old}) \tag{23}$$

$$- \sum_{z}^{N} o(z)b(z-\gamma_{k_0})$$

Maximize Target

When maximizing the conditional expectation from Equation 20 with respect to the target (o), the process is slightly different than the previous steps. To find the maximum likelihood estimate, the derivative of the conditional expectation with respect to a single pixel point z_0 in the true target, $o(z_o)$, is calculated. The results are shown in Equation 24.

$$\frac{\partial Q}{\partial o(z_0)} = \frac{\partial}{\partial o(z_0)} \sum_{k}^{K} \sum_{x}^{N} \sum_{z}^{N} \frac{\hat{o}^{old}(z)b(z-\gamma_k^{old})h(x-z-\alpha_k^{old})d_k(x)}{i_k^{old}(x)} \ln(o(z)b(z-\gamma_k)h(x-z$$

$$- \alpha_k)) - o(z)b(z-\gamma_k)h(x-z-\alpha_k)$$

$$= \sum_{k}^{K} \sum_{x}^{N} \sum_{z}^{N} \frac{\partial}{\partial o(z_0)} \frac{\hat{o}^{old}(z)b(z-\gamma_k^{old})h(x-z-\alpha_k^{old})d_k(x)}{i_k^{old}(x)} \ln(o(z)b(z \tag{24}$$

$$- \gamma_k)h(x-z-\alpha_k)) - \frac{\partial}{\partial o(z_0)} o(z)b(z-\gamma_k)h(x-z-\alpha_k)$$

Solving for the derivative of the first term of Equation 24 gives the results shown in Equation 25.

$$\frac{\partial}{\partial o(z_0)} \frac{\hat{o}^{old}(z)b\big(z - \gamma_k^{old}\big)h\big(x - z - \alpha_k^{old}\big)d_k(x)}{i_k^{old}(x)} \ln\big(o(z)b(z - \gamma_k)h(x - z - \alpha_k)\big)$$

$$= \frac{\hat{o}^{old}(z)b\big(z - \gamma_k^{old}\big)h\big(x - z - \alpha_k^{old}\big)d_k(x)}{i_k^{old}(x)} \frac{\partial \ln\big(o(z)\big)}{\partial o(z_0)} \qquad (25)$$

$$= \frac{\hat{o}^{old}(z)b\big(z - \gamma_k^{old}\big)h\big(x - z - \alpha_k^{old}\big)d_k(x)}{i_k^{old}(x)} \frac{1}{o(z)} \delta(z - z_0)$$

Additionally, the derivative of the second term of Equation 24 is shown in Equation 26.

$$\frac{\partial}{\partial o(z_0)} o(z)b(z - \gamma_k)h(x - z - \alpha_k) = b(z - \gamma_k)h(x - z - \alpha_k)\delta(z - z_0) \qquad (26)$$

Combining the two terms in Equation 25 and Equation 26, and then applying the sifting property, results in the final form of the conditional expectation that will be maximized shown in Equation 27.

$$\frac{\partial Q}{\partial o(z_0)} = \sum_k^K \sum_x^N \sum_z^N \frac{\hat{o}^{old}(z)b\big(z - \gamma_k^{old}\big)h\big(x - z - \alpha_k^{old}\big)d_k(x)}{i_k^{old}(x)} \frac{1}{o(z)} \delta(z - z_0)$$

$$- b(z - \gamma_k)h(x - z - \alpha_k)\delta(z - z_0) \qquad\qquad (27)$$

$$= \sum_k \sum_x \frac{\hat{o}^{old}(z_0)b\big(z_0 - \gamma_k^{old}\big)h\big(x - z_0 - \alpha_k^{old}\big)d_k(x)}{i_k^{old}(x)} \frac{1}{o(z_0)}$$

$$- b(z_0 - \gamma_k)h(x - z_0 - \alpha_k)$$

Equation 27 is set to zero to find when the maximum value will occur. This result is shown in Equation 28.

$$0 = \sum_k^K \sum_x^N \frac{\hat{o}^{old}(z_0)b\big(z_0 - \gamma_k^{old}\big)h\big(x - z_0 - \alpha_k^{old}\big)d_k(x)}{i_k^{old}(x)} \frac{1}{o(z_0)} - b(z_0 - \gamma_k)h(x - z_0 - \alpha_k) \qquad (28)$$

A rearrangement of terms in Equation 28 and simplifying the expression by removing the summed PSF results in Equation 29.

$$\sum_k^K b(z_0 - \gamma_k) = \sum_k^K \sum_x^N \frac{\hat{o}^{old}(z_0)b(z_0 - \gamma_k^{old})h(x - z_0 - \alpha_k^{old})d_k(x)}{i_k^{old}(x)} \frac{1}{o(z_0)} \tag{29}$$

Solving for the true target, $o(z_0)$, produces the final update equation shown in Equation 30. At each iteration of the algorithm the new estimate of the true target is identified as $\hat{o}^{new}(z_0)$. This solution is ideal because it could be used iteratively and updates the target at each iteration based only on past estimates of the unknown parameters $(\alpha_k^{old}, _k^{old}, \hat{o}^{old})$. Of possible concern is the summation of all the shifted beams in the denominator of Equation 30. However, mathematically a Gaussian approximation to long term beam wander as a result of atmospheric turbulence can be taken that eliminates the requirement to sum all of the beams individually [12].

$$\hat{o}^{new}(z_0) = \frac{\sum_k^K \sum_x^N \frac{\hat{o}^{old}(z_0)b(z_0 - \gamma_k^{old})h(x - z_0 - \alpha_k^{old})d_k(x)}{i_k^{old}(x)}}{\sum_k^K b(z_0 - \gamma_k)} \tag{30}$$

Expectation Maximization Update Equations

Expanding Equation 22, Equation 23 and Equation 30 to their two dimensional version results in the EM algorithm solution shown in Equation 31, Equation 32 and Equation 33.

33

$$\hat{o}^{new}(z_0, w_0)$$

$$= \frac{\sum_k^K \hat{o}^{old}(z_0, w_0) b(z_0 - \gamma_k^{old}, w_0 - \varepsilon_k^{old}) \sum_x^N \sum_y^N \frac{d(x,y)}{i_k^{old}(x,y)} h(x - z_0 - \alpha_k^{old}, y - w_0 - \beta_k^{old})}{\sum_k^K b(z_0 - \gamma_k, w_0 - \varepsilon_k)} \quad (31)$$

$$L_{\alpha_{k_0}, \beta_{k_0}} = \sum_z^N \sum_w^N \hat{o}^{old}(z, w) b(z - \gamma_{k_0}^{old}, w - \varepsilon_{k_0}^{old})$$

$$\times \sum_x^N \sum_y^N \frac{d(x,y)}{i^{old}(x,y)} h(x - z - \alpha_{k_0}^{old}, y - w - \beta_{k_0}^{old}) \ln\left(h(x - z - \alpha_{k_0}, y - w - \beta_{k_0})\right) \quad (32)$$

$$L_{\gamma_{k_0}, \varepsilon_{k_0}} = \sum_z^N \sum_w^N \hat{o}^{old}(z, w) b(z - \gamma_{k_0}^{old}, w - \varepsilon_{k_0}^{old}) \ln\left(b(z - \gamma_{k_0}, w - \varepsilon_{k_0})\right)$$

$$\times \sum_x^N \sum_y^N \frac{d_{k_0}(x,y)}{i_{k_0}^{old}(x,y)} h(x - z - \alpha_{k_0}^{old}, y - w - \beta_{k_0}^{old}) \quad (33)$$

$$- \sum_z^N \sum_w^N o(z, w) b(z - \gamma_{k_0}, w - \varepsilon_{k_0})$$

Examining these equations shows that a solution to solving for each of the parameters individually is mathematically possible by using an iterative process that would first update the object estimate, $\hat{o}^{new}$, then estimates the global shift parameters for each frame, α_k and β_k, and then estimates the beam shifts, γ_k and ε_k. However, a tractable solution could not be found in MATLAB during the implementation of the two maximum likelihood expressions solving for the beam and global shifts. The likely cause is that in both instances, MATLAB was unable to evaluate the natural log of the slightly shifting beam or PSF with enough accuracy to correctly estimate the shift. The non-linear properties of the natural log function and the fact that the beam and PSF approach zero on the tails caused the change between the beam or the PSF shifts from each frame

to be smaller than the machine's precision. It is possible that the algorithm might have converged to a solution if given more time or a computer with higher precision.

Although the pure EM approach did not completely work, the estimate for the target update worked and the fact that an EM solution exists for finding the shift values based only on past estimates suggest that solving for the target and the shifts independent is mathematically possible. To attempt to solve for the beam and global shifts a different cost function was studied.

3.2 Two Dimensional SSE Approach

Along with the target update from Equation 30, an iterative least squares likelihood cost function [2] was taken to solve for the global and beam shifts. The least squares algorithm steps the unknown parameter in each direction ($\pm\alpha, \beta$ or $\pm\gamma, \varepsilon$) separately and calculates the error at each location using Equation 34. The step that results in the least error is the direction to move the unknown parameter to.

$$SSE = \sum_{x}^{N}\sum_{y}^{N}\left(d_{k_0}(x,y) - i_{k_0}(x,y)\right)^2$$

(34)

As the algorithm iterates, each step brings the estimate closer to the actual solution. This technique is accomplished one frame at a time for first the global shifts and then for the beam shifts. When the minimum error is at the current location, the algorithm stops iterating. Figure 12 shows the flow of this technique for estimating the global shifts. Estimating the beam shift is not shown since it is exactly the same with γ and ε substituted in for α and β. The minimum step size at each iteration, *SS*, is defined in the algorithm and can be adjusted based on computation and accuracy requirements.
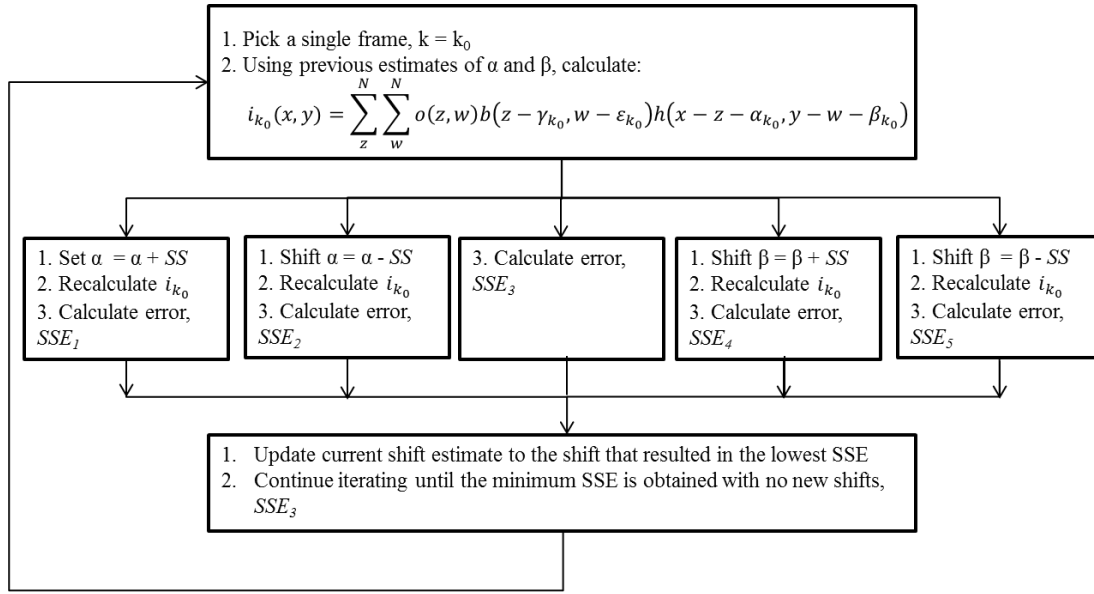
1. Pick a single frame, $k = k_0$
2. Using previous estimates of α and β, calculate:

$$i_{k_0}(x, y) = \sum_z^N \sum_w^N o(z, w) b(z - \gamma_{k_0}, w - \varepsilon_{k_0}) h(x - z - \alpha_{k_0}, y - w - \beta_{k_0})$$

1. Set $\alpha = \alpha + SS$ 2. Recalculate i_{k_0} 3. Calculate error, SSE_1	1. Shift $\alpha = \alpha - SS$ 2. Recalculate i_{k_0} 3. Calculate error, SSE_2	3. Calculate error, SSE_3	1. Shift $\beta = \beta + SS$ 2. Recalculate i_{k_0} 3. Calculate error, SSE_4	1. Shift $\beta = \beta - SS$ 2. Recalculate i_{k_0} 3. Calculate error, SSE_5

1. Update current shift estimate to the shift that resulted in the lowest SSE
2. Continue iterating until the minimum SSE is obtained with no new shifts, SSE_3

Figure 12: Two dimensional SSE algorithm flow

3.3 Testing Methods

The algorithm develop in this research was tested using both purely simulated data as well as a hybrid measured data set. These data sets were used to test and evaluate the performance of the proposed algorithm compared to current registration and deconvolution algorithms.

3.3.1 Simulated Data

The simulated images were generated in MATLAB for testing the proposed algorithm's ability to estimate the global and beam shifts while deconvoluting and registering the frames to obtain an estimate of the target. The simulated data was a set of 30 image frames. The target, previously shown in Figure 4, is a 512x512 pixel array of a mobile *United States Air Force* (USAF) resolution target board. The illuminating beam

36

was simulated to have a two dimensional unit Gaussian intensity profile with a standard deviation of 35 pixels as shown in Figure 13.
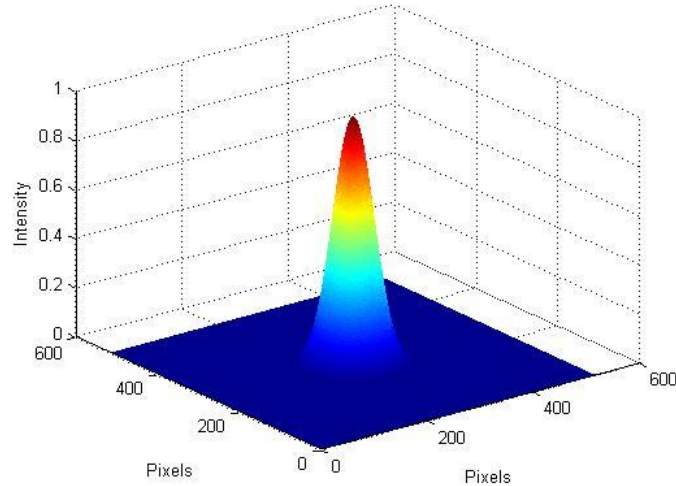

Figure 13: Simulated unit Gaussian illuminating beam

The simulated PSF contained a generic defocus error to mimic blurring of the target due to atmospheric turbulence. To simplify the problem, but still capture 89% of phase aberrations [14] only focus and tilt errors were included in the simulation.

The beam and global shifts in each frame due to atmospheric turbulence were chosen from the Gaussian distribution as zero mean with a standard deviation of 3 pixels for the global shift and a 7 pixels standard deviation for the beam using the Gaussian number generator function, *rand*, in MATLAB. This allowed enough movement in both the beam and scene to test the algorithm without entirely changing the detected image between frames. A wind velocity of 10 m/s across the aperture of the camera was assumed, this resulted in zero tilt correlation between frames of data and so the tilt at each frame is completely independent and uncorrelated with the previous frame [13].

There are two ways that speckle could be simulated. In the first scenario, a random phase screen is multiplied with the product of the beam and the target. This represents the phase delay expected in the reflected image due to the rough surface of the target. Then using Fourier transforms to simulate propagation, the phase delay resulted in speckle at the image plane. However, an alternate approach was used when creating simulated data for this research. First, an image was simulated in MATLAB assuming completely incoherent light was being used. Then speckle noise was added to the predicted image at the detector plane using the MATLAB *icdf* function to add negative binomial noise with 30 degrees of freedom to each frame to represent the speckle expected from partially coherent light. The *icdf* function in MATLAB adds the desired random distribution to the input variable when given the mean value and a certain number of degrees of freedom, *M*, related to how coherent the light is which effects the degree of intensity fluctuations [10]. This process simulates speckled data that contains the same statistics as would be expected using the correct physical model described in the first scenario since the expected value of multiple speckled images that are averaged is the image expected if using an incoherent light source.

The background noise was generated using the Poisson number generator with a mean of 20 photons and added to the detected image. The parameters used in the simulated data are summarized in Table 1.

Table 1 Simulation setup parameters

Parameter	Value
Image size	512 x 512 pixels
Beam width standard deviation	35 pixels
Global shift standard deviation	3 pixels
Beam shift standard deviation	7 pixels
Aperture diameter, D	2 mm
Time between pulses	.1 s
Wind velocity across aperture	10 m/s
Intensity degrees of freedom, M	30
Mean background noise, $\bar{B}$	20 photons
Detected image, max photon count	250 photons
Number of frames in data set	30 frames

Shown in Figure 14 is an example of four simulated consecutive frames of data. The different beam and global shifts are apparent between frames as well as the distinctive speckle pattern among each frame.

Frame 1
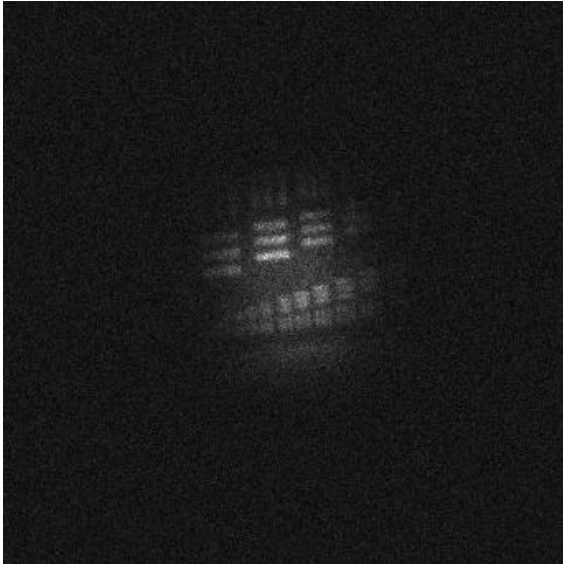
Frame 2
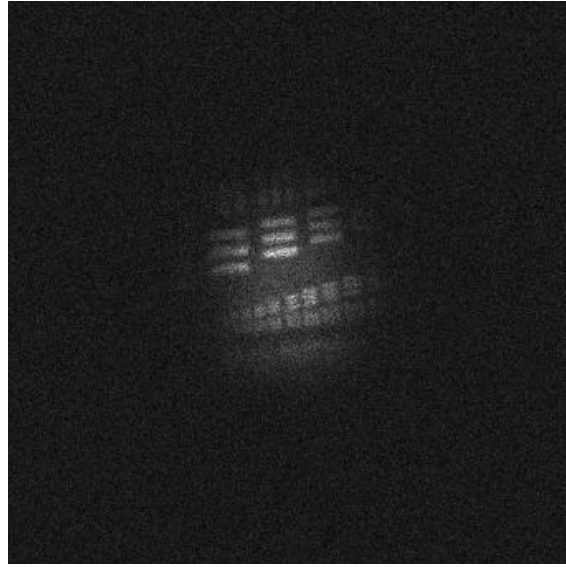
Frame 3

Frame 4

Figure 14: Four frames of simulated data

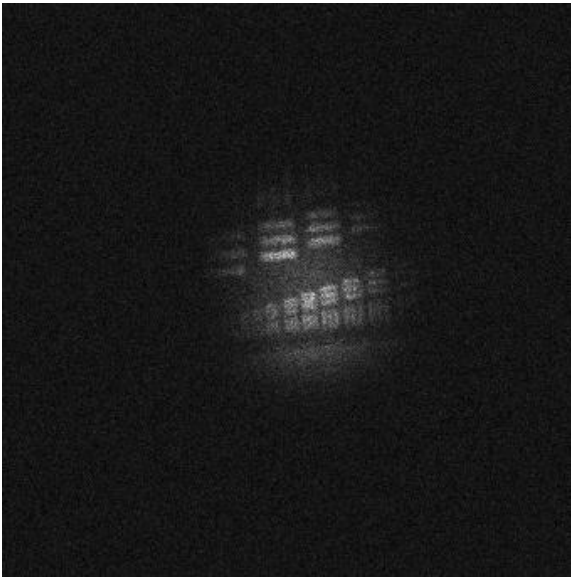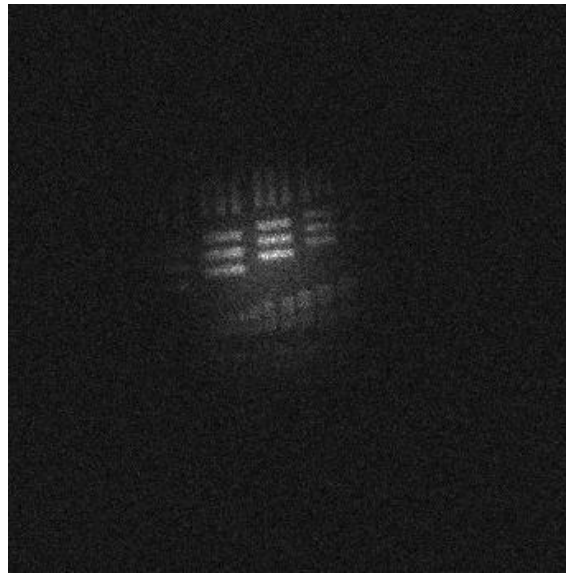### 3.3.2 Measured Data

It was unfeasible to collect measured data that contained controlled beam shifting as well as global shifting in the laboratory environment available for this research. To compensate, a hybrid approach was taken to collect measured data. An imaging system was set up in the laboratory with the computer display screen at the focal plane of a focusing lens, 4.5 inches in front of the camera as shown in Figure 15. The imaging system captured 20 frames of the same simulated data frame and then the next frame of data was displayed on the computer screen. The 20 frames of data were averaged to obtain a higher SNR on the detected image.
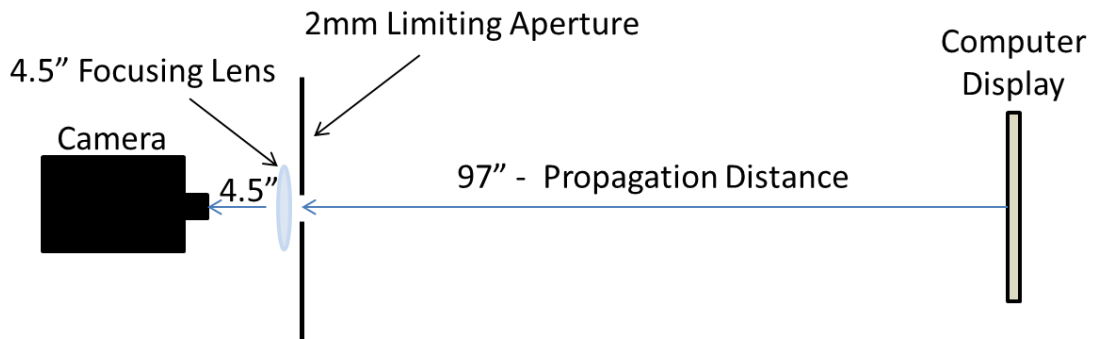
Figure 15: Laboratory setup

The data displayed on the computer screen contained the target multiplied by a shifted beam and that result shifted again to simulate the scene shift. This was generated using MATLAB in a similar manner as was described in the simulated data with several variations. First, the target multiplied by the beam was not convolved with a PSF, the convolution with the PSF occurred naturally in the setup due to the 2mm aperture. Second, the negative binomial distribution of speckle was simulated by adding Gamma

distributed noise using the MATLAB *icdf* function. Gamma distributed noise was used to simulate the intensity fluctuation expected due to the rough surface target [10]. The naturally occurring Poisson process (camera photon counting) with a mean that has a Gamma distribution, results in a negative binomial distribution expected for speckle noise. Additionally, background noise was not added to the image since this will occur naturally. Shown in Figure 16 are the first four frames of measured data after 20 frames of identical data are averaged to improve the SNR of the frames to be used by the algorithm.
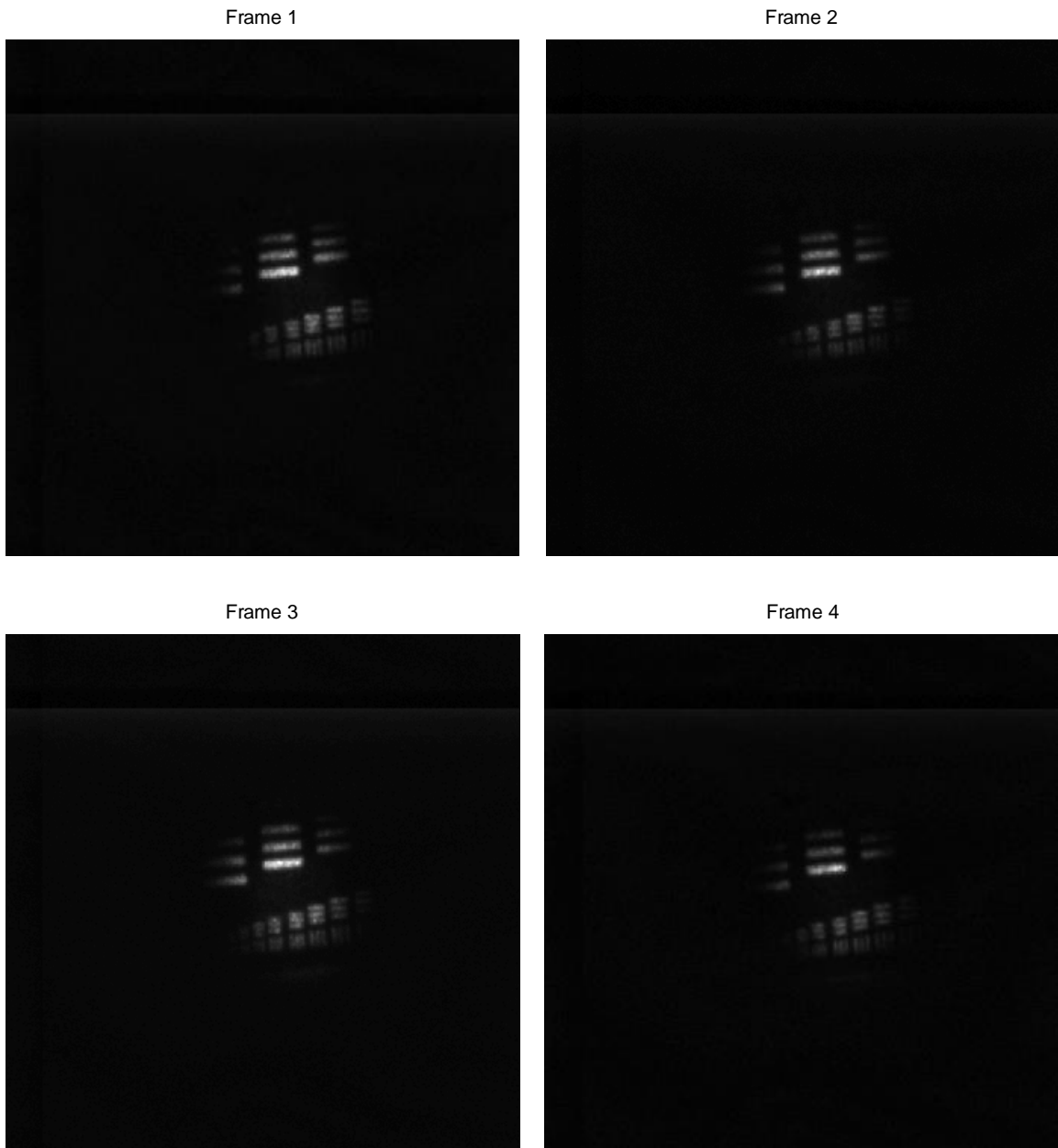
Frame 1

Frame 2

Frame 3

Frame 4

Figure 16: Four frames of measured data

Collecting measured data using this hybrid approach has the key advantage in that the truth data is known because the beam and global shifts were defined in MATLAB. This approach can still be called measured data because an optical system is used to

capture the data, the speckle noise and background noise is truly random and the PSF is convoluted naturally in this set-up. However, the value for all parameters will not be known exactly as is the case in a simulated environment. The parameters for the measured data set up are summarized in Table 2.

Table 2 Measured data parameters

Parameter	Value
Width of camera captured image	512 x 512 pixels
Display window physical size	19.5 x 19.5 cm
Display size, N	512 pixels
Beam width standard deviation	35 pixels
Beam shift standard deviation	7 pixels
Global shift standard deviation	3 pixels
Coherence parameter, M	30
Number of identical frames averaged	20
Camera integration time	0.1 sec
Aperture diameter, D	2 mm
Focusing lens focal length, f_ℓ	4.5 in
Distance from lens to display	97 in
Number of frames in data set	30 frames
Pixel pitch on camera	16 um
Background radiation, $\bar{B}$ (measured)	1036 photons

Knowing the relationship between a pixel represented on the computer display and a pixel captured by the camera system is an important piece of information in this hybrid approach. Following principles of optics systems [9], the *optics magnification* factor can be calculated using the property of similar triangles with the measurements shown in Figure 15 and Table 2. This information allows a shift in the MATLAB environment to be translated into a shift in the detected image. Shown in Equation 35, the magnification ratio, Δ_r, is calculated as 1.104. Thus a shift of 1 pixel in MATLAB

and displayed on the computer screen would correspond to a shift of 1.104 pixels in the image detected by the camera.

$$\Delta_r = \frac{\text{size of pixel on display}}{\text{size of pixel on CCD}} \times \text{optics magnification} = \frac{\left(\frac{19.5\ cm}{512}\right)}{16\ um} \times \frac{4.5"}{97"} = 1.104 \tag{35}$$

3.3.3 Comparison Criteria

Several criteria were used to evaluate the performance of the algorithm using the measured and simulated data. For both the simulated and measured data, the error of the estimated shift parameters, E', at each frame of data can be calculated using Equation 36 when the true shifts are known. Additionally, this error can be calculated for both scenarios where the beam is being tracked in the algorithm at each frame and when the beam is considered to be stationary. To be successful, the proposed algorithm needs to provide a better estimate of the global shifts when the beam position is tracked. This would result in a decrease in the registration error and thus an image with a higher SNR and greater resolution when multiple frames are averaged.

$$E'_\alpha(k) = \alpha_{true}(k) - \hat{\alpha}(k)$$
$$E'_\beta(k) = \beta_{true}(k) - \hat{\beta}(k)$$
$$E'_\gamma(k) = \gamma_{true}(k) - \hat{\gamma}(k) \tag{36}$$
$$E'_\varepsilon(k) = \varepsilon_{true}(k) - \hat{\varepsilon}(k)$$

Using the simulated data, the estimated image, $\hat{o}(z, w, k)$, at each iteration k, can be compared to the known true target, $o(z, w)$, to calculate the *root mean squared error* (RMSE) at each iteration using Equation 37 where N is the number of pixels in the image array. The RMSE can be calculated using both the scenario where the beam is tracked and with the beam tracking off. A marked improvement in RMSE when the beam is tracked would indicate the algorithm provides better performance than standard image registration algorithms that do not track beam wander.

$$RMSE(k) = \sqrt{\frac{\sum_{w=1}^{N} \sum_{z=1}^{N} \hat{o}(z, w, k) - o(z, w)}{N^2}}$$

(37)

IV. Results and Analysis

This chapter presents the results of applying the algorithm developed in *Chapter III* to both the simulated and measured data sets. In both situations, the error in the estimated shift parameter is evaluated. In the simulated environment, the RMSE of the estimated image is calculated at each iteration. These metrics are analyzed to determine if the proposed algorithm provides an improved performance over cross-correlation, which is the most commonly used image registration technique.

4.1 Simulated Data Results

Using simulated data created as described in *Chapter III*, the proposed algorithm was used to estimate the shifts and true target using the parameters shown in Table 3. The scale or step size for estimating the shifts was set to a quarter of a pixel. Changing the step size allows for a tradeoff between better estimates of the shifts but with a significantly longer execution time as the step size is decreased.

Table 3 Algorithm parameters

Parameter	Value
Number of frames of data	30
Pixel shift scale	¼ pixel
Max number of iterations	50

Using simulated data with the algorithm tracking the beam produced an estimated image of the target shown in Figure 17 after 50 iterations. The exercise was repeated using the same data set and parameters except the ability to track the beam disabled. This resulted in the estimated image shown in Figure 18. Visually these two results look

similar with the exception that the estimated image when tracking the beam is slightly larger than the estimate obtained when the beam is not tracked. This is due to the beam being estimated at each frame and data on the edges of each frame not being lost when multiple frames are averaged.
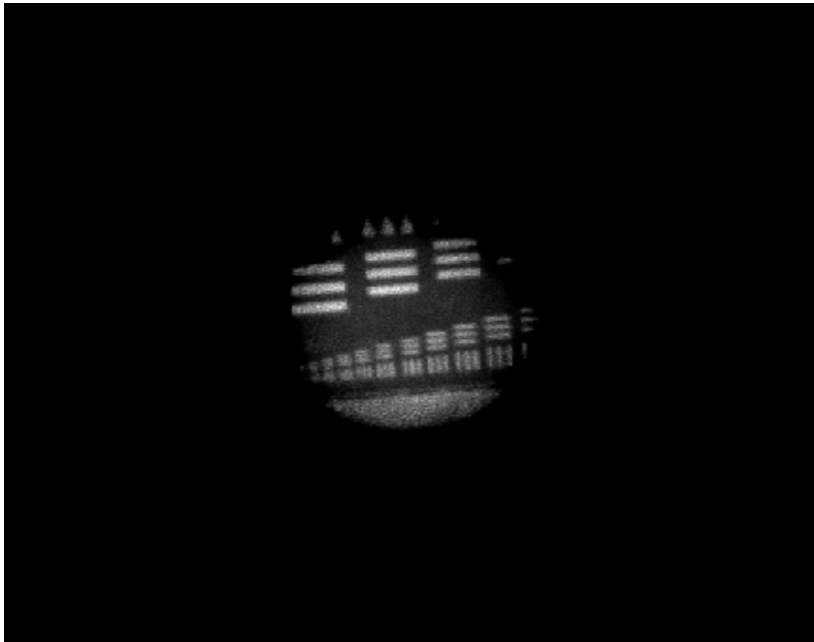
Figure 17: Estimated target using simulated data – beam tracking on
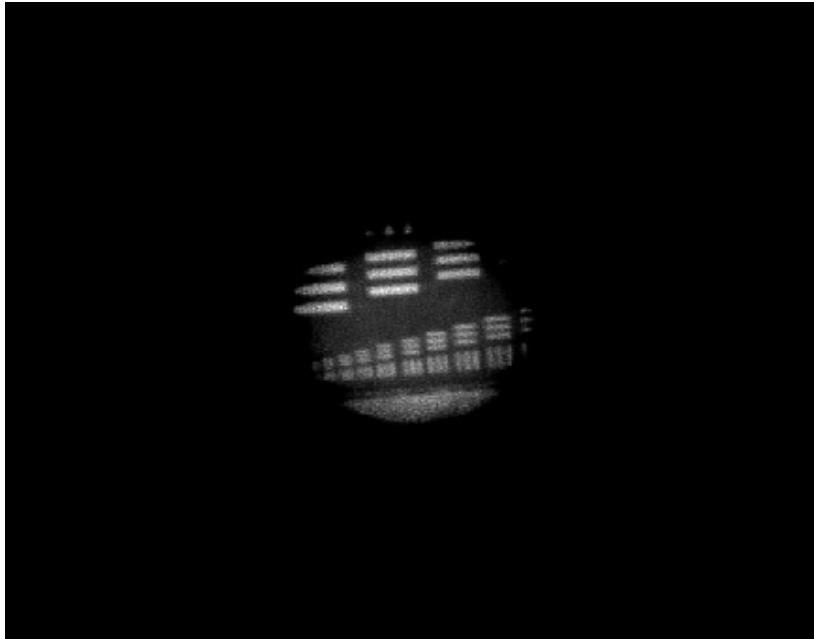
Figure 18: Estimated target using simulated data – beam tracking off

The RMSE of the estimated image after each iteration was calculated using Equation 37 and the results are shown in Figure 19. After the 50th iteration, the RMSE was 27.9 photons with beam tracking on and 32.4 with beam tracking off. This represents a 13.8% improvement in RMSE performance when the beam is tracked at each frame.
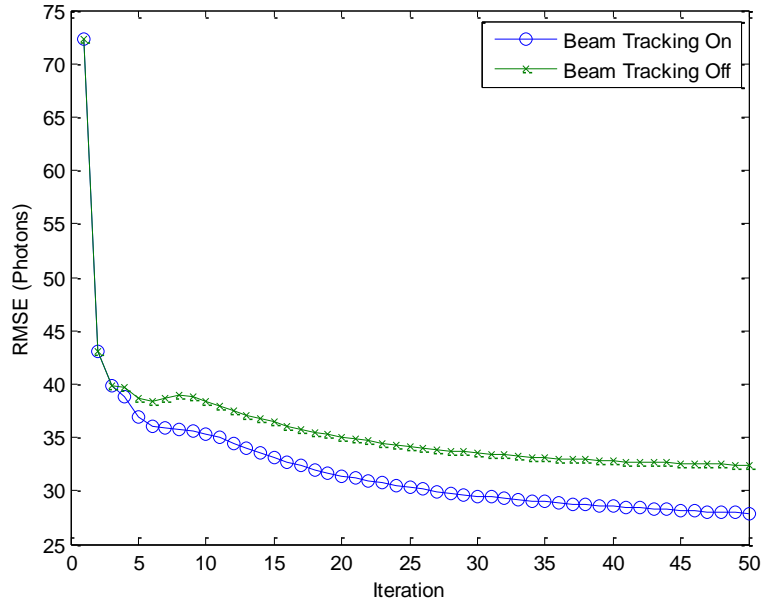
Figure 19: RMSE - Simulated data photon error at each iteration

The estimated shifts from the algorithm, given explicitly in Appendix B along with the true shifts, are summarized by using Equation 36 to compute the error. The calculated error in the estimated shift for each frame of data when compared to the true shifts is shown for each parameter (α, β, γ and ε) in Figure 20, Figure 21, Figure 22 and Figure 23. When examining the beam shift error in Figure 22 and Figure 23 there is only one set of data plotted because when the algorithm is not estimating the beam shift, the error of the estimated beams position is irrelevant.

Figure 20: Error in shift estimate for α using simulated data

Figure 21: Error in shift estimate for β using simulated data

Figure 22: Error in shift estimate for γ using simulated data
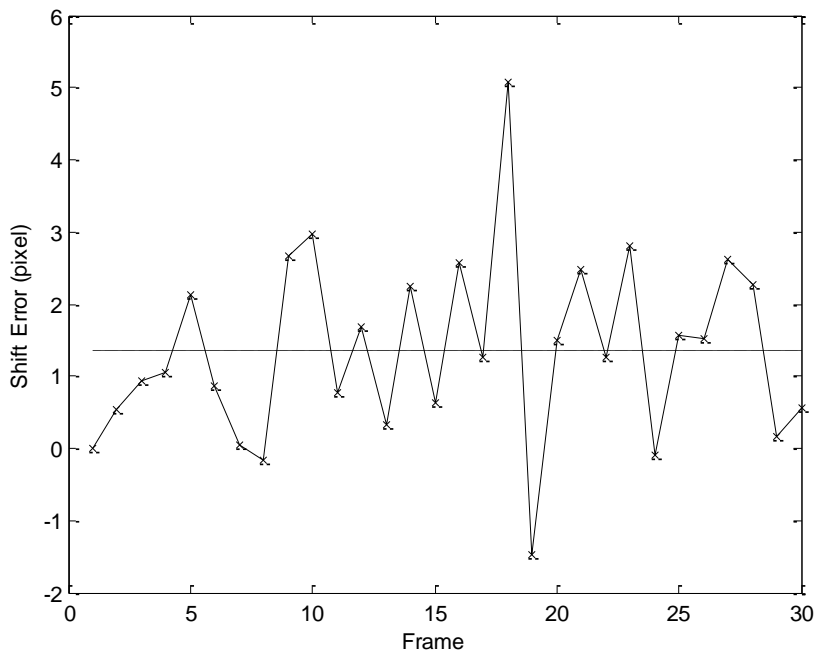
Figure 23: Error in shift estimate for ε using simulated data

52

Analyzing the information provided in the previous graphs show that when using simulated data, the algorithm provides superior results when the beam tracking feature is enabled. The difference in the algorithm's ability to track better in one direction versus the other is likely a result of the phys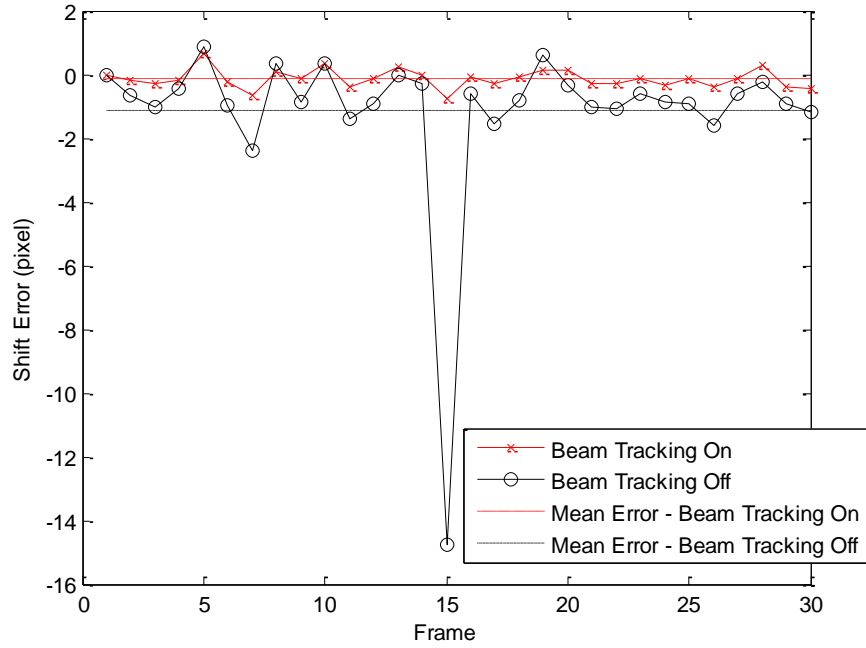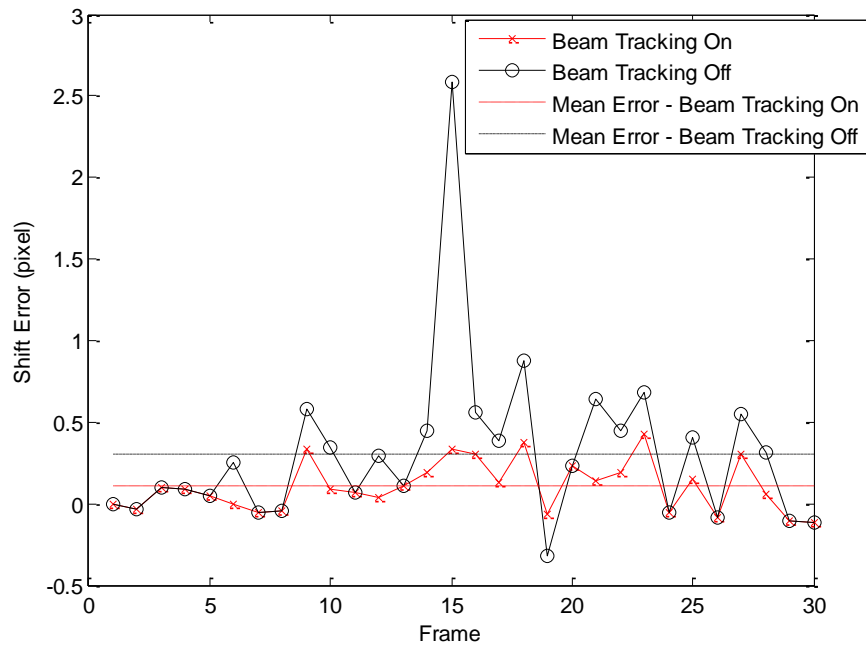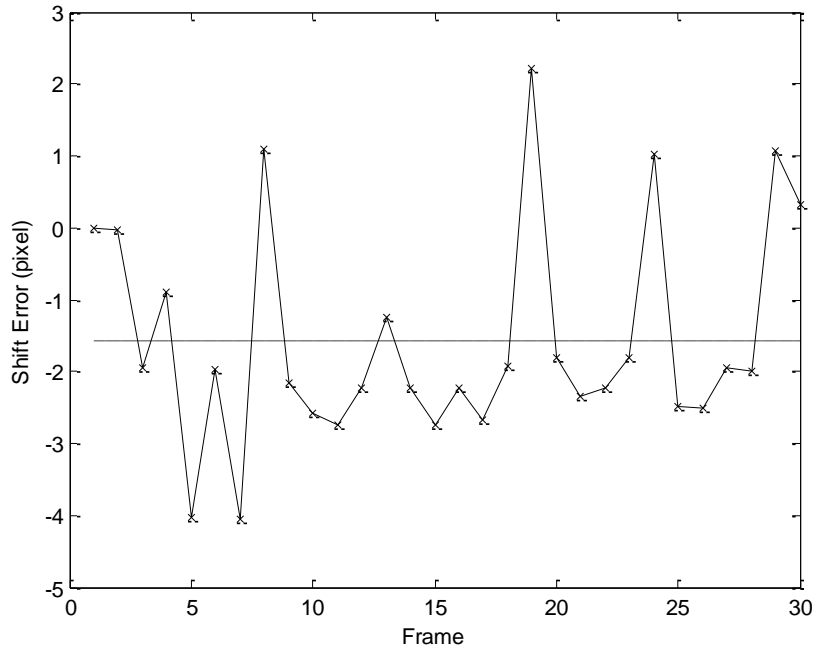ical properties of the target. One concern is the outlier in frame 15 that appears in Figure 21 and Figure 22. The global shift estimate for this frame is wildly off from all other estimates. This is likely a result of the combination of a large beam shift and the fact that the bar charts on the target at many locations look nearly identical. Due to the beam illuminating a different bar chart on the target in that frame caused the global shift to be off. To ensure this wasn't skewing the results, the mean of the error in the estimated shift parameters is summarized in Table 4 with the 15th frame removed from the mean calculations. When using the proposed algorithm to estimate the beam shift, the registration error decreased by 88% in the α direction and 45% in the β direction.

Table 4 Mean error in the shift estimates

Parameter	Mean Error (pixels)	Mean Error 15th Frame Removed	Decrease in Error
α – beam tracking on	-0.08	-0.07	88%
α – beam tracking off	-1.07	-0.60	
β – beam tracking on	0.16	0.16	45%
β – beam tracking off	0.36	0.29	
γ – beam tracking on	-1.57	-1.48	
ε – beam tracking on	1.36	1.34	

4.2 Measured Data

Using the setup described in Figure 15 and Table 2, the algorithm was used to estimate the shifts and target using the same parameters from the simulated data and shown in Table 3. The estimated images produced by the algorithm are shown in Figure 24 and Figure 25. Visually comparing Figure 24 and Figure 25, the tracked beam case in Figure 24 is clearly better resolved than the untracked case in Figure 25. Additionally, when the beam is tracked the estimated image is slightly larger than the image estimated when the beam is not tracked. This is shown more clearly in Figure 26 which is looking only at the fringes of the estimate image. There is clearly more information on the fringes when the beam is being tracked.
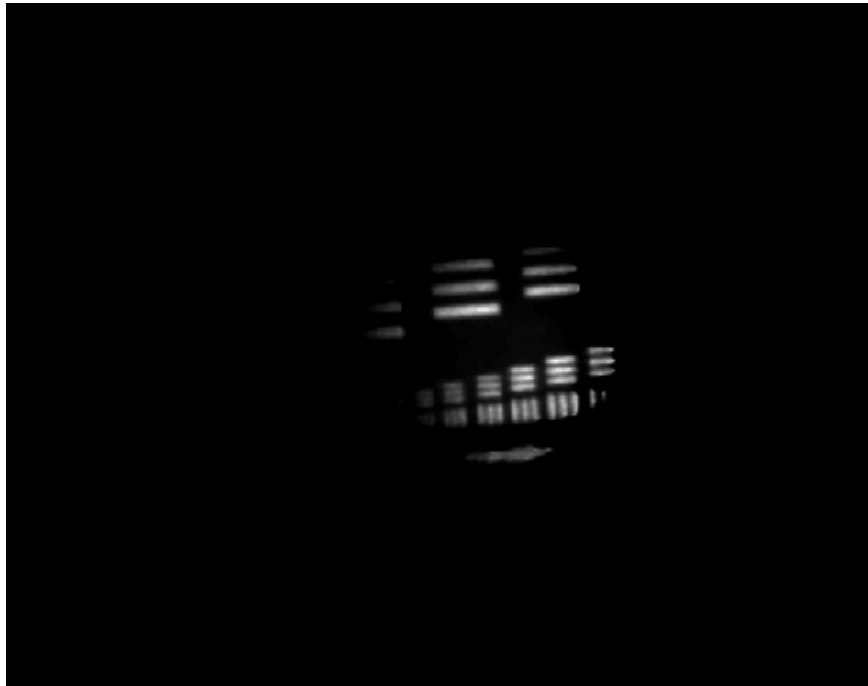
Figure 24: Estimated target using measured data – beam tracking on
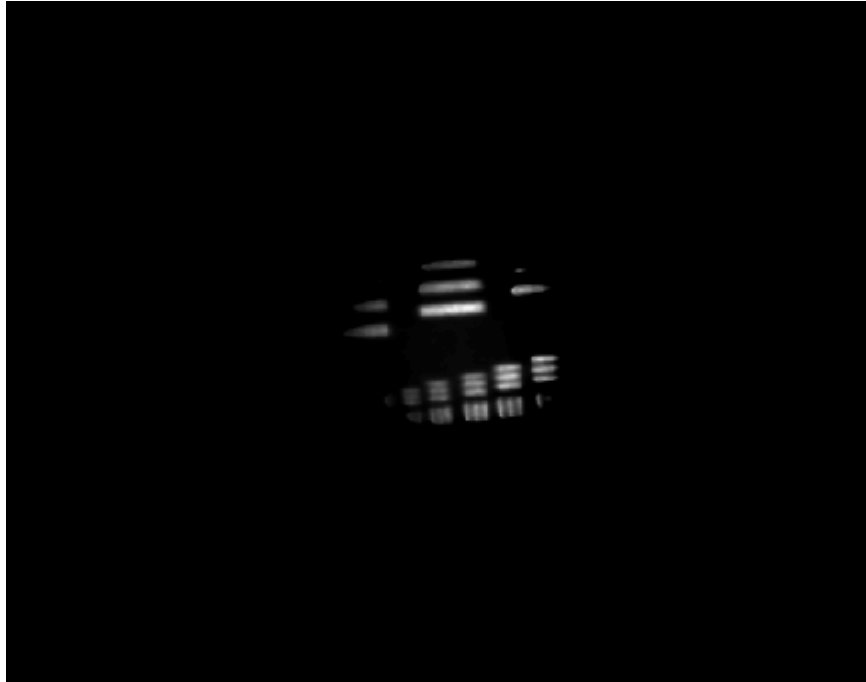
Figure 25: Estimated target using measured data – beam tracking off
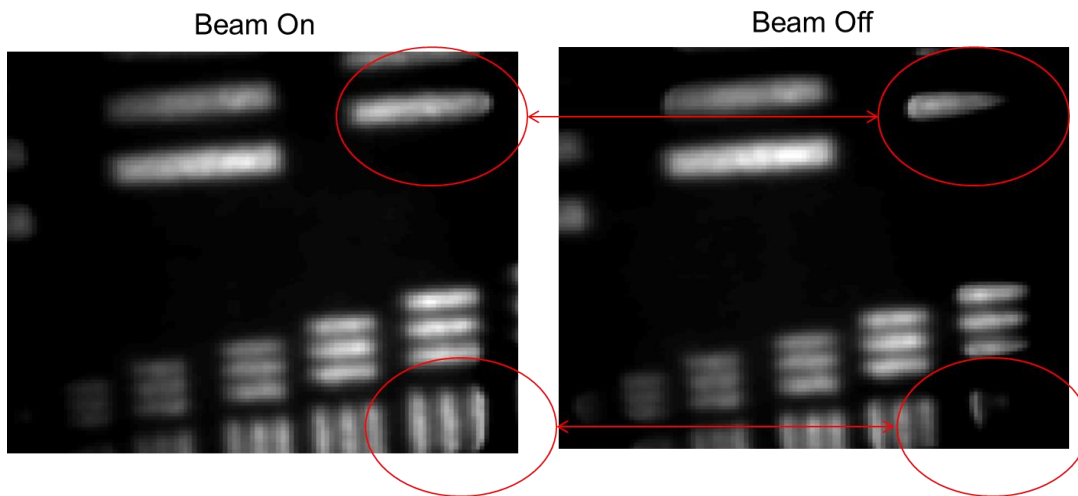
Figure 26: Difference in estimated target at the fringes

The estimated shifts, given in Appendix B, are summarized by using Equation 36 to compute the error at each frame when compared to the true shift and is shown in

Figure 27, Figure 28, Figure 29 and Figure 30. The true shifts, controlled in the MATLAB environment are the same shifts used in the simulated data. However, they need to be scaled by 1.104 as was found in Equation 35 to obtain the true shifts in the measured data. Similar to the experimental data, frame 15 appears to be an outlier and the mean is also calculated with that frame removed and is also summarized in Table 5.
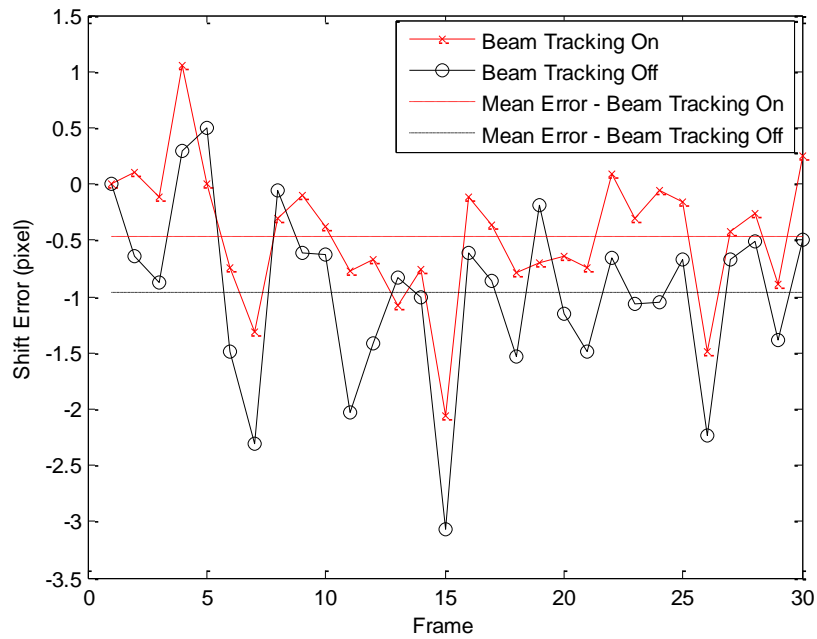
Figure 27: Error in shift estimate for α using measured data
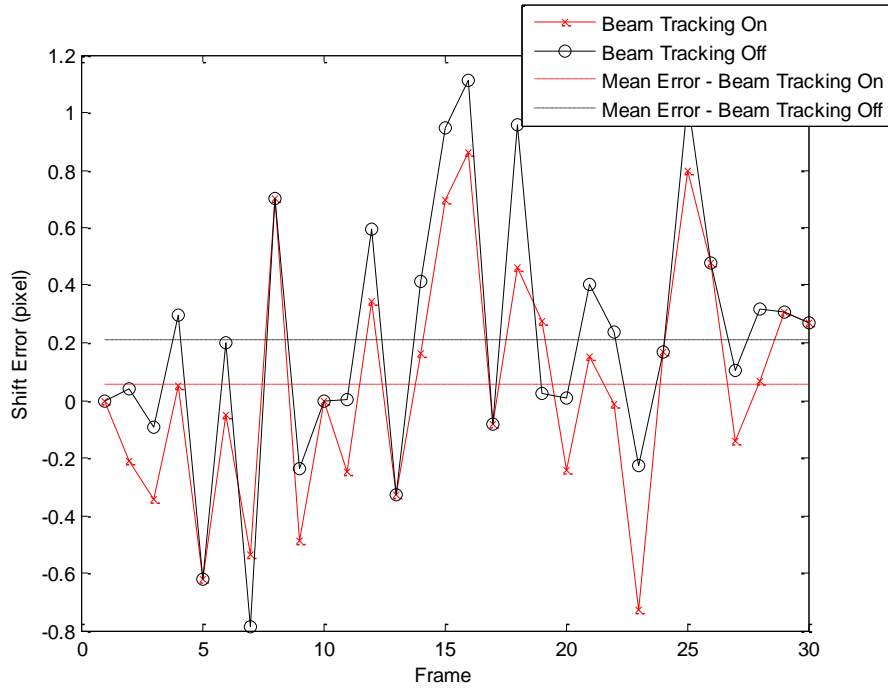
Figure 28: Error in shift estimate for β using measured data
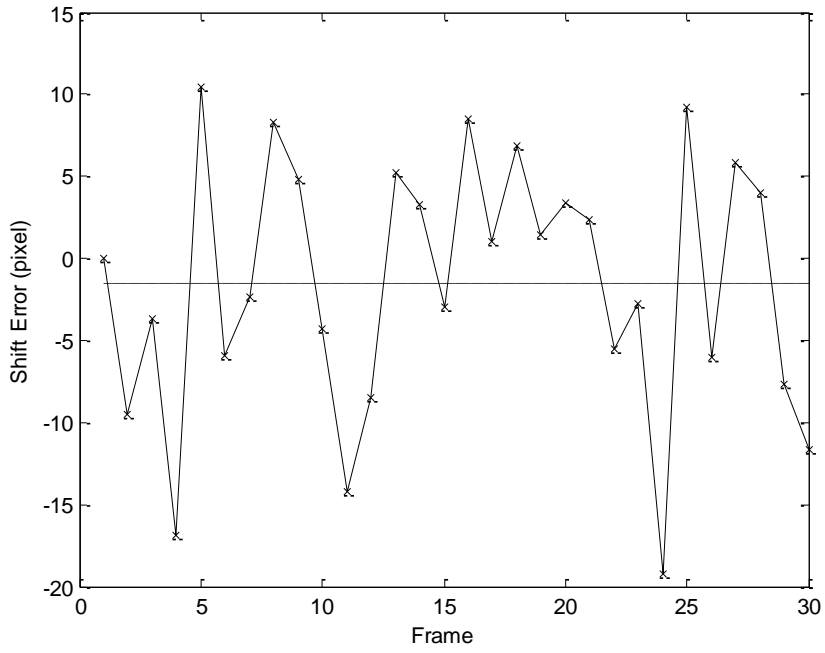
Figure 29: Error in shift estimate for γ using measured data
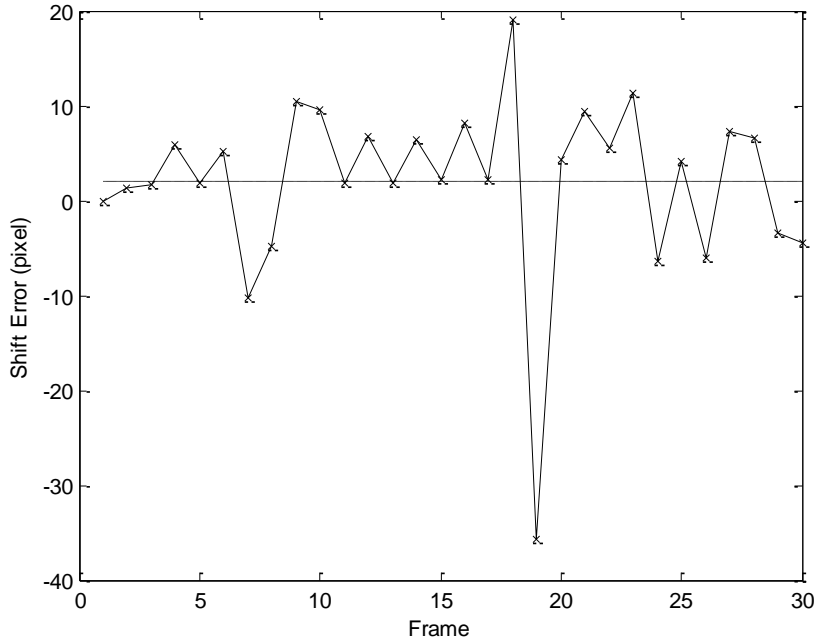
Figure 30: Error in shift estimate for ε using measured data

Table 5 Mean error in the shift estimates using measured data

Parameter	Mean Error (pixels)	Mean Error 15th Frame Removed	Decrease in Error
α – beam tracking on	-0.46	-0.39	55%
α – beam tracking off	-0.96	-0.86	
β – beam tracking on	0.06	0.04	78%
β – beam tracking off	0.21	0.18	
γ – beam tracking on	-1.55	-1.45	
ε – beam tracking on	2.05	1.98	

Analyzing the information provided in the previous graphs show that in most frames the algorithm provides a better estimate of the shifts when the beam is tracked. Looking at the mean error with the 15th frame removed shows a 55% and 78% reduction in the α and β shift error respectively when the beam is tracking. Thus a lower RMSE and higher resolution image would be expected when the beam tracking is on and the

images are averaged. Due to the scaling from the camera and uncertainties in measured data, a RMSE of the photon error cannot be calculated since the true image is not known.

4.3 Analysis of Results

Examining both measured and simulated data, the proposed algorithm provides an improvement in registration performance when the beam is tracked. The reduction in shift error is similar between the simulated and experimental data sets. This is significant due to the additional challenges associated with using measured data. Specifically, the PSF and the summation of the beam shifts from Equation 31 cannot be known exactly when working with measured data. Mathematically, the beam sum term can be simplified since the summation of numerous Gaussian beams that are shifted results in another Gaussian beam that has a larger standard deviation [6]. However this mathematical simplification will not be equal to the exact sum of the shifted beams when there are a limited number of frames of data as is the case in these data sets. These unknown factors along with the noise introduced in the measured data create a situation that is not as ideal as working in a purely simulated environment.

A stopping criterion for the beam and global shift estimates and image deconvolution was necessary in this experiment. It was observed that once the estimated shifts were identical to the previous iteration, the estimates would not further improve but instead slowly diverge from the solution. This was due to the algorithm's design in that at each iteration it attempts to make the estimated image look more like the detected image which includes noise. Thus, a stopping criterion was set that once the estimated

shifts didn't change from the previous estimates, the algorithm stopped updating the shift estimates.

Of additional interest in the results was the ability of the algorithm to create a larger image when the beam is tracked. This resulted in more information on the target being estimated. This is a direct result of tracking the beam at each frame instead of considering that the beam is stationary. As the amount of beam wander increases, this advantage proportionally increases however the algorithm's error will increase if there is too much beam wander to accurately register frames.

To further validate the algorithm's increased performance abilities, the shift estimates from the proposed algorithm are compared to the estimates obtained from a cross-correlation registration algorithm [2]. The results are shown in Figure 31, Figure 32, Figure 33 and Figure 34 show the significant improvement in registration performance the proposed algorithm provides over a cross-correlation algorithm used for image registration using both simulated and measured data. Similar to the previous results, frame 15 could be considered an outlier and thus the mean error with that frame removed is shown in Table 6 using the simulated data and in Table 7 using the experimental data. Both data sets show a 19% to 83% reduction in shift registration error when using the proposed algorithm to register frames.
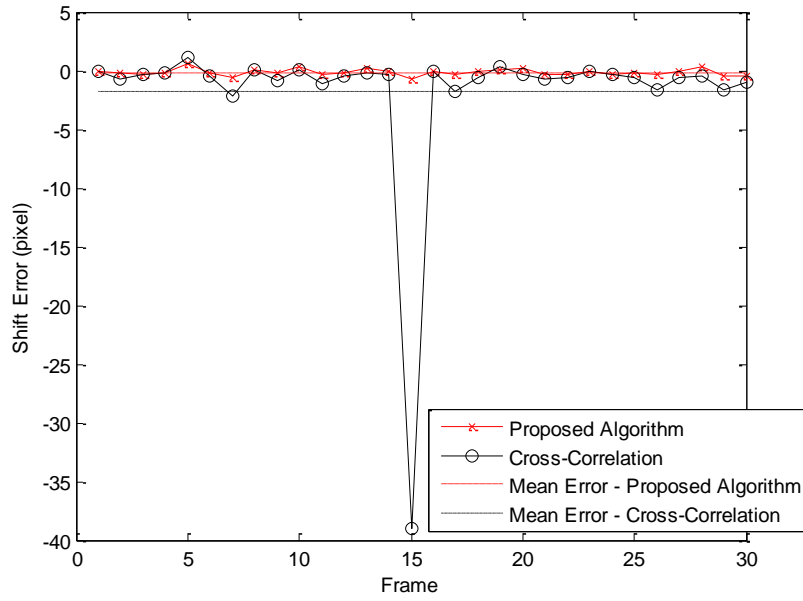
Figure 31: Error in shift estimate for α using simulated data
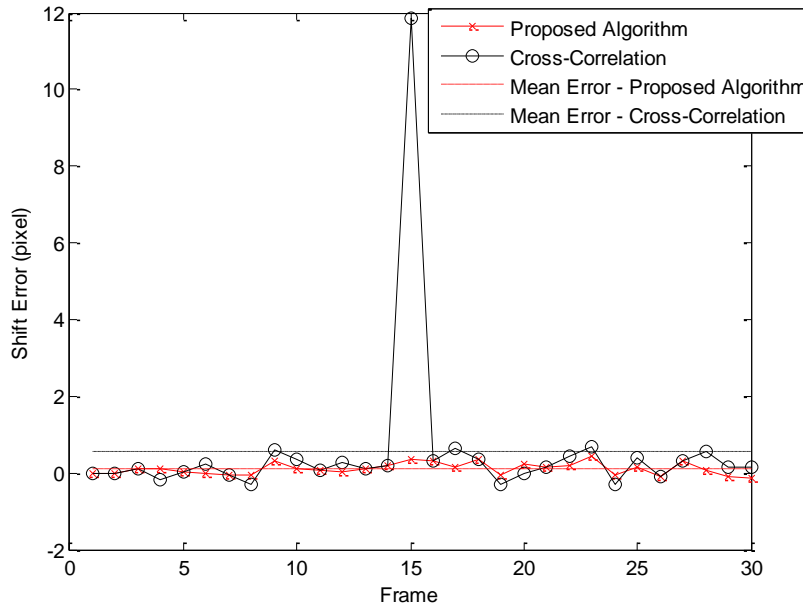
Figure 32: Error in shift estimate for β using simulated data
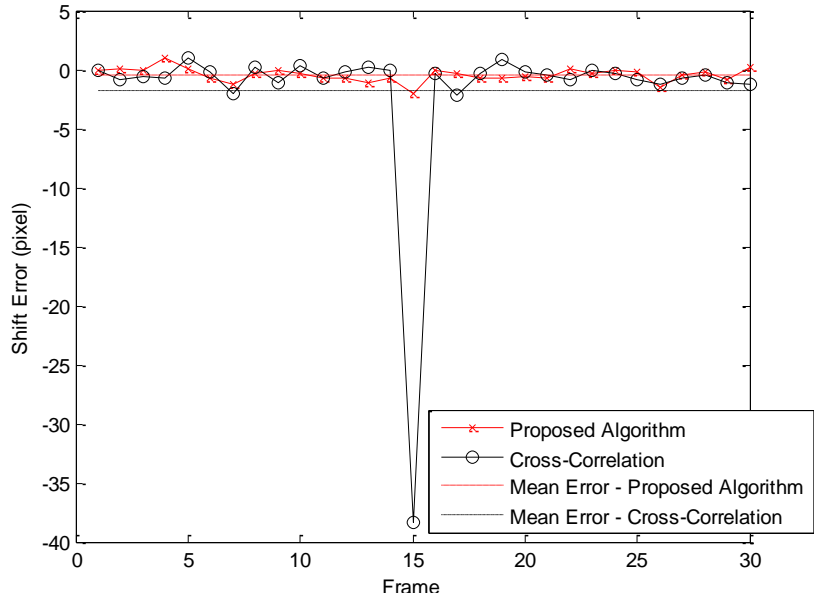
Figure 33: Error in shift estimate for α using measured data
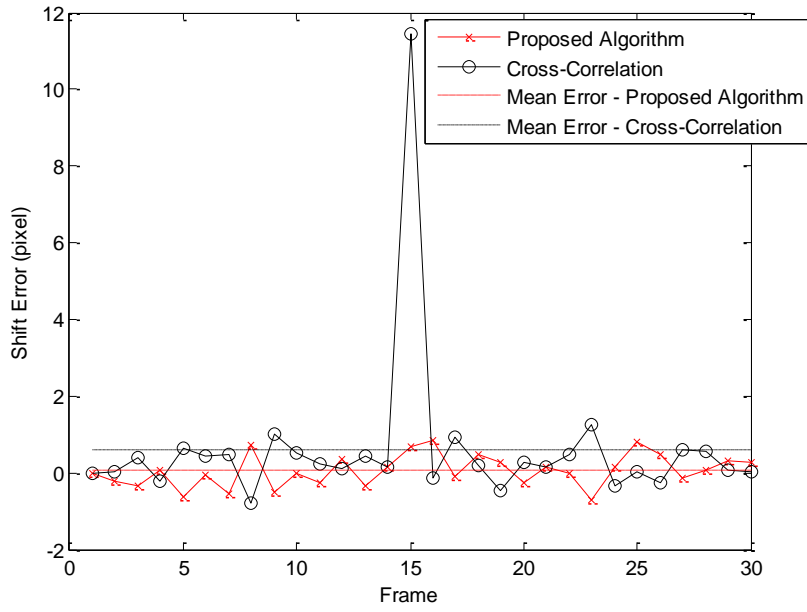
Figure 34: Error in shift estimate for β using measured data

Table 6 Mean error in the shift estimates using simulated data

Parameter	Mean Error (pixels)	15th Frame Removed Mean Error (pixels)	Decrease in Error
α – proposed algorithm	-0.14	-0.11	79%
α – cross-correlation	-1.82	-0.52	
β – proposed algorithm	-0.11	-0.09	43%
β – cross-correlation	0.55	0.16	

Table 7 Mean error in the shift estimates using measured data

Parameter	Mean Error (pixels)	15th Frame Removed Mean Error (pixels)	Decrease in Error
α – proposed algorithm	-0.46	-0.39	19%
α – cross-correlation	-1.76	-0.48	
β – proposed algorithm	0.06	-0.04	83%
β – cross-correlation	0.61	0.23	

V. Conclusions and Recommendations

This section details the conclusions that can be made from the results and analysis of this research. Additionally, future related follow-on research to this effort is presented.

5.1 Conclusions of Research

The results from this research prove that under certain circumstances beam wander caused by atmospheric turbulence can be tracked independently of scene shifting. This results in a superior registered image after post-processing as well as tracking information for the beam and scene separately. The algorithm proposed in this research was proven using both simulated and a measured data set to provide an improved performance when compared to a cross-correlation standard image registration algorithm which does not track beam wander but considers it to be stationary.

Unique to this research was the use of a hybrid approach to collecting measured data. Data was displayed on a computer screen so that the true shifts in the beam and scene could be controlled and known. A camera was used to capture the scene displayed on the screen thus unknown parameters associated with true measured data such as noise are intact. This hybrid approach allowed measured data to be captured in a space limited laboratory environment that would have taken several kilometers on a test range to collect.

The capabilities of this algorithm have potential significant defense applications. The ability to reduce registration error results in an image that will have greater resolution providing the end user with more information on the target. The defense and intelligence applications could include damage assessment of a laser weapon strike or

more detailed information on a target in space situational awareness and LADAR imaging scenarios. Specifically, the ability of the algorithm to provide greater scene tracking capability in the presence of beam wander could have applications to improving the performance of the USAF's airborne laser weapon system.

5.2 Recommendations for Future Research

The algorithm provides an improved performance in registration but just how significant is this improvement to various applications is not known. An analysis on the capabilities this improved performance could provide is a topic that could be addressed. Additionally, this algorithm as written does not provide real time feedback. In future work, the processing time could possibly be improved to provide near real time tracking information. This could result in significantly improving beam and scene tracking information for defense and commercial applications.

Future follow-on work to this research could emphasize reducing the restraints on the assumptions made to scope the level of work. Currently, the algorithm only has the ability to work with a fixed and known PSF. A blind deconvolution approach to estimate the PSF at each iteration would improve the performance and applications of the algorithm. Another factor is that different types of registration error are not included in this algorithm and are both possible and likely. These include scaling or off axis rotation of the scene between images. Future work that reduces or eliminates these constraints would improve performance and broaden its relevance.

Lastly, future work could be done on using true measured data from a test range and testing the algorithm's ability to prove it can provide superior performance with this

data. The hybrid approach to collecting the measured data used in this research may find skeptics who are leery that the algorithm would not perform as well if true measured data was to be used.

<center>**Appendix A**</center>

This appendix provides a detailed derivation of the first term in the conditional expectation of the log-likelihood function in *Chapter III*.

A.1 Conditional Expectation of the Complete Data Log Likelihood

The expression shown below in Equation 38 was the original equation to be simplified and solved for in deriving of the conditional expectation of the log-likelihood function in *Chapter III*.

$$\mathrm{E}\big[\widetilde{d_k}(x,z)\ln\big(o(z)b(z-\gamma_k)h(x-z-\alpha_k)\big)\,|\,\hat{o}^{old},d_k(x),\alpha_k^{old},\gamma_k^{old}\big] \tag{38}$$

First, two statistically independent Poisson random variables, d_1 and d_2, are defined as shown in Equation 39 and Equation 40. The new Poisson random variable, d_1, is one frame of the complete data at a single point z_0. The Poisson random variable, d_2, is the sum of all the frames and pixel points in the complete data except for the point in d_1, the Poisson background noise is also added to this sum.

$$d_1 = \tilde{d}(x,z_0) \tag{39}$$

$$d_2 = \sum_{k}^{K}\sum_{z}^{N}\tilde{d}(x,z) - \tilde{d}(x,z_0) + B(x) \tag{40}$$

These two random variables, d_1 and d_2, are defined to have some mean, m, as shown in Equation 41 and Equation 42.

$$\mathrm{E}[d_1] = m_1 \tag{41}$$

$$\mathrm{E}[d_2] = m_2 \tag{42}$$

<center>67</center>

Looking back at Equation 10, the incomplete data is related to d_1 and d_2 as shown in Equation 43.

$$d(x) = \sum_k^K d_k(x) = \sum_k^K \sum_z^N \widetilde{d_k}(x,z) + B(x) = d_1 + d_2 \tag{43}$$

Using the Poisson PMF, the joint probability of the random variables d_1 and d_2 with means m_1 and m_2 is given in Equation 44.

$$P(d_1, d_2) = \left(\frac{m_1^{d_1} e^{-m_1}}{d_1!}\right)\left(\frac{m_2^{d_2} e^{-m_2}}{d_2!}\right) \tag{44}$$

The variable d_2 can be removed from Equation 44 to allow simplification using the equality in Equation 45. The new joint probability is shown in Equation 46.

$$d_2 = d - d_1 \tag{45}$$

$$P(d, d_1) = \left(\frac{m_1^{d_1} e^{-m_1}}{d_1!}\right)\left(\frac{m_2^{d-d_1} e^{-m_2}}{(d-d_1)!}\right) \tag{46}$$

Using Bayes theorem [6], the conditional expectation of d_1 is found and simplified in Equation 47.

$$
\begin{aligned}
P(d_1|d) &= \frac{P(d, d_1)}{P(d)} = \frac{\left(\frac{m_1^{d_1} e^{-m_1}}{d_1!}\right)\left(\frac{m_2^{d-d_1} e^{-m_2}}{(d-d_1)!}\right)}{\frac{(m_1 + m_2)^d e^{-(m_1+m_2)}}{d!}} = \frac{(d!)m_1^{d_1}}{(m_1 + m_2)^d (d_1!)} \frac{m_2^{d-d_1}}{(d-d_1)!} \\
&= \frac{(d!)m_1^{d_1}}{(m_1 + m_2)^{(d_1+d-d_1)}(d_1!)} \frac{m_2^{d-d_1}}{(d-d_1)!} \\
&= \frac{(d!)\left(\frac{m_1}{(m_1 + m_2)}\right)^{d_1}}{(d_1!)} \frac{\left(\frac{m_2}{(m_1 + m_2)}\right)^{d-d_1}}{(d-d_1)!}
\end{aligned} \tag{47}
$$

The final form of the conditional expectation in Equation 47 is similar to the PMF of a binomial random variable shown in Equation 48. The binomial PMF describes the probability of getting exactly n successes in k trials for an event with a probability of

success p [6]. The mean of a binomial is shown in Equation 49. The relationships between Equation 47 and the binomial PMF are shown in Table A.1.

$$P(n, p) = \frac{n!}{k! \, (n-k)!} p^k (1-p)^{n-k} \tag{48}$$

$$E[\text{Binominal}(n, p)] = np \tag{49}$$

Table A.1 Relationship between the conditional expectation log likelihood function and the binomial PMF

Number of trials	d
Number of success	d_1
Probability of success	$\dfrac{m_1}{(m_1 + m_2)}$
Probability of failure	$\dfrac{m_2}{(m_1 + m_2)}$
Mean	$d\left(\dfrac{m_1}{m_1 + m_2}\right)$

Converting back to the original notation in Equation 38, the conditional expectation of the complete data log-likelihood is shown in Equation 50.

$$
\begin{aligned}
&E\big[\widetilde{d_k}(x,z) \ln\big(o(z)b(z - \gamma_k)h(x - z - \alpha_k)\big) \mid \hat{o}^{old}, d_k(x), \alpha_k^{old}, \gamma_k^{old}\big] \\
&= E\big[\widetilde{d_k}(x,z) | \hat{o}^{old}, d_k(x), \alpha_k^{old}, \gamma_k^{old}\big] \ln\big(o(z)b(z - \gamma_k)h(x - z - \alpha_k)\big) \\
&= \frac{d(x)\hat{o}^{old}(z)b\big(z - \gamma_k^{old}\big)h\big(x - z - \alpha_k^{old}\big)}{i_k^{old}(x)} \ln\big(o(z)b(z - \gamma_k)h(x - z - \alpha_k)\big)
\end{aligned}
\tag{50}
$$

Where shown again for easy reference,

$$i_k^{old}(x) = \sum_z^N \hat{o}^{old}(z,w)b\big(z - \gamma_k^{old}\big)h\big(x - z - \alpha_k^{old}\big). \tag{51}$$

Appendix B

This appendix provides the true shifts in the MATLAB environment, as well as the shifts estimated by the algorithm using both the simulated data and measured data.

B.1 Simulated Data Results

The true shift and the estimated shifts from the algorithm when using simulated data are given explicitly in Table B.1, B.2, B.3 and B.4.

B.2 Measured Data Results

The scaled true shifts and the estimated shifts from the algorithm when using measured data are given explicitly in Table B.5, B.6, B.7 and B.8.

Table B.1 True and estimated shifts for α using simulated data

Frame #	True Shift	Estimate - Beam Tracking On	Estimate - Beam Tracking Off
1	0.00	0.00	0.00
2	2.17	2.00	1.50
3	3.29	3.00	2.25
4	5.18	5.00	4.75
5	1.36	2.00	2.25
6	-2.28	-2.50	-3.25
7	-0.85	-1.50	-3.25
8	-0.85	-0.75	-0.50
9	2.14	2.00	1.25
10	-2.61	-2.25	-2.25
11	-3.61	-4.00	-5.00
12	-2.34	-2.50	-3.25
13	-4.24	-4.00	-4.25
14	-2.72	-2.75	-3.00
15	-7.21	-8.00	-22.00
16	2.83	2.75	2.25
17	3.28	3.00	1.75
18	-2.70	-2.75	-3.50
19	-4.37	-4.25	-3.75
20	-2.14	-2.00	-2.50
21	-2.96	-3.25	-4.00
22	3.56	3.25	2.50
23	-0.63	-0.75	-1.25
24	-0.63	-1.00	-1.50
25	2.65	2.50	1.75
26	-3.87	-4.25	-5.50
27	0.62	0.50	0.00
28	0.23	0.50	0.00
29	-5.10	-5.50	-6.00
30	3.18	2.75	2.00

Table B.2 True and estimated shifts for β using simulated data

Frame #	True Shift	Estimate - Beam Tracking On	Estimate - Beam Tracking Off
1	0.00	0.00	0.00
2	-0.72	-0.75	-0.75
3	-3.10	-3.00	-3.00
4	0.41	0.50	0.50
5	-5.80	-5.75	-5.75
6	-2.00	-2.00	-1.75
7	-5.20	-5.25	-5.25
8	5.04	5.00	5.00
9	-4.33	-4.00	-3.75
10	-1.59	-1.50	-1.25
11	-1.82	-1.75	-1.75
12	1.96	2.00	2.25
13	-3.11	-3.00	-3.00
14	0.31	0.50	0.75
15	3.91	4.25	6.50
16	4.44	4.75	5.00
17	-2.88	-2.75	-2.50
18	1.63	2.00	2.50
19	1.57	1.50	1.25
20	-2.73	-2.50	-2.50
21	-0.14	0.00	0.50
22	-0.44	-0.25	0.00
23	-5.93	-5.50	-5.25
24	0.30	0.25	0.25
25	3.60	3.75	4.00
26	1.84	1.75	1.75
27	-3.05	-2.75	-2.50
28	-0.06	0.00	0.25
29	0.86	0.75	0.75
30	1.12	1.00	1.00

Table B.3 True and estimated shifts for γ using simulated data

Frame #	True Shift	Estimate - Beam Tracking On
1	0.00	0.00
2	-7.93	-8.75
3	-12.33	-15.50
4	-7.36	-9.00
5	8.67	5.50
6	-10.48	-13.50
7	-23.82	-30.25
8	2.65	4.00
9	-10.77	-14.00
10	2.35	0.00
11	-16.59	-21.00
12	-12.53	-16.00
13	-1.38	-2.75
14	-5.02	-7.75
15	-26.14	-31.50
16	-8.20	-11.25
17	-16.65	-21.00
18	-9.15	-12.00
19	3.45	6.00
20	-6.08	-8.50
21	-11.04	-14.50
22	-13.20	-16.75
23	-8.36	-11.00
24	-9.56	-9.50
25	-12.05	-15.75
26	-18.41	-22.75
27	-7.77	-10.50
28	-4.09	-6.50
29	-9.83	-9.75
30	-12.80	-13.75

Table B.4 True and estimated shifts for ε using simulated data

Frame #	True Shift	Estimate - Beam Tracking On
1	0.00	0.00
2	0.64	1.25
3	3.91	5.25
4	4.94	6.50
5	6.47	9.25
6	7.62	9.25
7	-10.73	-11.75
8	-2.81	-3.25
9	14.17	18.25
10	12.07	16.25
11	2.94	4.00
12	9.84	12.50
13	4.25	5.00
14	12.28	15.75
15	11.69	13.50
16	13.33	17.25
17	9.54	11.75
18	21.98	29.25
19	-7.99	-10.25
20	8.42	10.75
21	15.03	19.00
22	9.31	11.50
23	15.40	19.75
24	-5.83	-6.50
25	11.30	14.00
26	-2.29	-1.00
27	12.63	16.50
28	11.34	14.75
29	-2.87	-3.00
30	-3.92	-3.75

Table B.5 True and estimated shifts for α using measured data

Frame #	True Shift	Estimate - Beam Tracking On	Estimate - Beam Tracking Off
1	0.00	0.00	0.00
2	2.39	2.50	1.75
3	3.62	3.50	2.75
4	5.70	6.75	6.00
5	1.50	1.50	2.00
6	-2.51	-3.25	-4.00
7	-0.93	-2.25	-3.25
8	-0.94	-1.25	-1.00
9	2.36	2.25	1.75
10	-2.87	-3.25	-3.50
11	-3.97	-4.75	-6.00
12	-2.58	-3.25	-4.00
13	-4.67	-5.75	-5.50
14	-2.99	-3.75	-4.00
15	-7.93	-10.00	-11.00
16	3.11	3.00	2.50
17	3.61	3.25	2.75
18	-2.97	-3.75	-4.50
19	-4.81	-5.50	-5.00
20	-2.35	-3.00	-3.50
21	-3.26	-4.00	-4.75
22	3.91	4.00	3.25
23	-0.69	-1.00	-1.75
24	-0.69	-0.75	-1.75
25	2.92	2.75	2.25
26	-4.26	-5.75	-6.50
27	0.68	0.25	0.00
28	0.26	0.00	-0.25
29	-5.61	-6.50	-7.00
30	3.50	3.75	3.00

Table B.6 True and estimated shifts for β using measured data

Frame #	True Shift	Estimate - Beam Tracking On	Estimate - Beam Tracking Off
1	0.00	0.00	0.00
2	-0.79	-1.00	-0.75
3	-3.40	-3.75	-3.50
4	0.45	0.50	0.75
5	-6.38	-7.00	-7.00
6	-2.20	-2.25	-2.00
7	-5.71	-6.25	-6.50
8	5.55	6.25	6.25
9	-4.76	-5.25	-5.00
10	-1.75	-1.75	-1.75
11	-2.00	-2.25	-2.00
12	2.16	2.50	2.75
13	-3.42	-3.75	-3.75
14	0.34	0.50	0.75
15	4.30	5.00	5.25
16	4.89	5.75	6.00
17	-3.17	-3.25	-3.25
18	1.79	2.25	2.75
19	1.73	2.00	1.75
20	-3.01	-3.25	-3.00
21	-0.15	0.00	0.25
22	-0.49	-0.50	-0.25
23	-6.52	-7.25	-6.75
24	0.33	0.50	0.50
25	3.96	4.75	5.00
26	2.02	2.50	2.50
27	-3.36	-3.50	-3.25
28	-0.07	0.00	0.25
29	0.94	1.25	1.25
30	1.23	1.50	1.50

Table B.7 True and estimated shifts for γ using measured data

Frame #	True Shift	Estimate - Beam Tracking On
1	0.00	0.00
2	-8.73	-18.25
3	-13.56	-17.25
4	-8.10	-25.00
5	9.54	20.00
6	-11.53	-17.50
7	-26.20	-28.50
8	2.91	11.25
9	-11.84	-7.00
10	2.58	-1.75
11	-18.25	-32.50
12	-13.78	-22.25
13	-1.52	3.75
14	-5.52	-2.25
15	-28.75	-31.75
16	-9.02	-0.50
17	-18.32	-17.25
18	-10.07	-3.25
19	3.79	5.25
20	-6.68	-3.25
21	-12.15	-9.75
22	-14.52	-20.00
23	-9.20	-12.00
24	-10.52	-29.75
25	-13.26	-4.00
26	-20.25	-26.25
27	-8.55	-2.75
28	-4.50	-0.50
29	-10.81	-18.50
30	-14.08	-25.75

Table B.8 True and estimated shifts for ε using measured data

Frame #	True Shift	Estimate - Beam Tracking On
1	0.00	0.00
2	0.70	2.00
3	4.31	6.00
4	5.44	11.25
5	7.11	9.00
6	8.39	13.50
7	-11.80	-22.00
8	-3.09	-8.00
9	15.59	26.00
10	13.28	22.75
11	3.23	5.00
12	10.82	17.50
13	4.67	6.50
14	13.51	20.00
15	12.86	15.00
16	14.67	22.75
17	10.50	12.75
18	24.17	43.25
19	-8.79	-44.50
20	9.26	13.50
21	16.53	26.00
22	10.24	15.75
23	16.95	28.25
24	-6.41	-12.75
25	12.43	16.50
26	-2.52	-8.50
27	13.89	21.25
28	12.48	19.00
29	-3.15	-6.50
30	-4.31	-8.75

Bibliography

[1]   A. Bovik, Handbook of Image and Video Processing, Burlington MA: Elsevier Academic Press, 2005.

[2]   A. MacDonald, E. Armstrong and S. Cain, "Comparison of Registration Techniques for Speckle Suppression in 2D LADAR Image Sequences," *Applications of Digital Image Processing,* vol. 5558, no. XXVII, pp. 202-213, 2004.

[3]   A. P. Dempster, N. M. Laird and D. B. Rubin, "Maximium likelihood from incomplete data via the em algorithm," *Journal of the Royal Statistical Soc. ,* no. 39, pp. 1-38, 1977.

[4]   D. Dayton, S. Browne, J. Gonglewski, S. Sandven, J. Gallegos and M. Shilko, "Long-range laser illuminated imaging: analysis and experimental demonstrations," *Soc. of Photo-Optical Instrumentation Engineers,* pp. 1001-1009, June 2001.

[5]   D. R. Sabo, "Development of a robust optical image registration algorithm for negating speckle noise effects in coherent images generated by a laser imaging system," 2005.

[6]   G. Casella and R. L. Berger, Statistical Inference, Belmont CA: Wadsworth Publishing Company, 1990.

[7]   G. R. Ayers and J. C. Dainty, "Iterative blind deconvolution method and its applications," *Opt. Lett.,* no. 13, pp. 547-549, 1988.

[8]   H. Weichel, Laser Beam Propagation in the Atmosphere, Bellingham WA: SPIE Optical Engineering Press, 1990.

[9]   J. W. Goodman, Introduction to Fourier Optics, Greenwood Village CO: Roberts & Company, 2005.

[10] J. W. Goodman, Statistical Optics, New York NY: John Wiley & Sons Inc, 1985.

[11] K. P. Vitayaudom, Analysis of Non-Uniform Gain for Control of a Deformable

Mirror in an Adaptive-Optics System, AFIT: Master's thesis, 2008.

[12] L. C. Andrews and R. L. Phillips, Laser Beam Propagation through Random Media, Bellingham WA: SPIE Press, 2005.

[13] R. D. Richmond and S. C. Cain, Direct-Detection LADAR Systems, Bellingham WA: SPIE Press, 2010.

[14] R. J. Noll, "Zernike polynomials and atmospheric turbulence," *J. Opt. Soc. Am. 66,* pp. 207-211, 1976.

REPORT DOCUMENTATION PAGE

1. REPORT DATE *(DD-MM-YYYY)* 21 Mar 2013	2. REPORT TYPE Master's Thesis	3. DATES COVERED *(From – To)* 27 Aug 2011 – 21 Mar 2013

4. TITLE AND SUBTITLE Laser Illuminated Imaging: Multiframe Beam Tilt Tracking and Deconvolution Algorithm	5a. CONTRACT NUMBER
	5b. GRANT NUMBER
	5c. PROGRAM ELEMENT NUMBER

6. AUTHOR(S) Becker, David J, Captain, USAF	5d. PROJECT NUMBER
	5e. TASK NUMBER
	5f. WORK UNIT NUMBER

7. PERFORMING ORGANIZATION NAMES(S) AND ADDRESS(S) Air Force Institute of Technology Graduate School of Engineering and Management (AFIT/EN) 2950 Hobson Way, Building 640 WPAFB OH 45433	8. PERFORMING ORGANIZATION REPORT NUMBER AFIT-ENG-13-M-07

9. SPONSORING/MONITORING AGENCY NAME(S) AND ADDRESS(ES) Intentionally Left Blank	10. SPONSOR/MONITOR'S ACRONYM(S)
	11. SPONSOR/MONITOR'S REPORT NUMBER(S)

12. DISTRIBUTION/AVAILABILITY STATEMENT

DISTRIBUTION STATEMENT A. APPROVED FOR PUBLIC RELASE; DISTRIBUTION UNLIMITED

13. SUPPLEMENTARY NOTES

14. ABSTRACT

A laser-illuminated imaging system operating in the presence of atmospheric turbulence will encounter several sources of noise and diffraction induced errors. As the beam propagates, turbulence induced tilt will cause the beam to wander off axis from the target. This is especially troublesome when imaging satellites, since most turbulence is closer to the Earth's surface and greatly affects the beam in the early stages of propagation. Additionally, the returning beam convolved with the target will encounter turbulence induced tilt that appears as apparent movement of the target between image frames. This results in varying beam intensities at the target surface between imaging frames that can affect registration algorithms and tracking. In this research effort, an algorithm using expectation maximization and least squares techniques was developed that has the ability to separately estimate both the tilt of the pulsed laser beam and the apparent movement of the object between incoherent frames and produce a superior image estimate of the target and provide tracking information. The results from this algorithm can be used to reduce the effects of beam wander and increase the SNR of post-processed images.

15. SUBJECT TERMS
 LADAR, Beam Wander, Image Registration, Deconvolution, Expectation Maximization

16. SECURITY CLASSIFICATION OF:			17. LIMITATION OF ABSTRACT	18. NUMBER OF PAGES	19a. NAME OF RESPONSIBLE PERSON Cain, Stephen C., Civ, USAF, (ENG)
a. REPORT U	b. ABSTRACT U	c. THIS PAGE U	UU	89	19b. TELEPHONE NUMBER *(Include area code)* (937) 255-3636, x 4716 (Stephen.Cain@afit.edu)